Chaos, Solitons and Fractals 209 (2026) 118539

Contents lists available at ScienceDirect

Chaos, Solitons and Fractals

journal homepage: www.elsevier.com/locate/chaos

Contact selection chaos of two analytical Gömböcs under biharmonic vertical excitation

Dong Feng [a,*]

[a] Faculty of Civil Engineering, RWTH Aachen University, Mies-van-der-Rohe-Stra﷽e 1, 52074, Aachen, Germany

ARTICLE INFO

Keywords:
Gömböc
Contact selection
Biharmonic excitation
Strange attractor
Analytical Gömböc morphology

ABSTRACT

Chaotic rocking of homogeneous Gömböc bodies on a vertically excited support is investigated by explicitly embedding two analytical Gömböc morphologies within a spherical radial surface description. The instantaneous contact point is obtained from a global height minimization over the rotated surface, which couples attitude evolution to a contact selection mechanism that can switch between competing minimizing branches. Under biharmonic vertical excitation, this coupling generates strong nonlinearity and leads to period multiplication, intermittency, crisis transitions, and strange attractors. The two analytical morphologies, distinguished by their phase functions on the spherical parameter domain, produce different contact-branch organizations and therefore different routes to chaotic responses under identical forcing conditions. Chaotic behavior is characterized using stroboscopic Poincaré sampling and maximal Lyapunov exponents, and its onset is related to separatrix splitting in a reduced near-saddle description. The results indicate that smooth mono-monostatic morphology can act as an intrinsic chaos generator through contact selection rather than through impacts or multi-contact constraints.

1. Introduction

Mono-monostatic convex bodies form a rare class of homogeneous solids that possess exactly one stable equilibrium and one unstable equilibrium when resting on a horizontal plane [1–7]. The Gömböc is the best known representative of this class and is notable because it is close to a sphere while still preserving the minimal equilibrium structure [8]. This combination makes the Gömböc a natural object for studying how subtle geometric features can control macroscopic mechanical behavior [9–11]. Beyond its mathematical interest, self-righting convex bodies are relevant to passive stabilization concepts in engineering [12–14], to shape-induced motion in granular media [15–17] or vibrating environments [18–20], and to broader questions in nonlinear dynamics where geometry acts as a source of nonlinearity even in the absence of joints or compliant elements [21–23].

Rocking and rolling of rigid bodies have long served as archetypal problems in nonlinear dynamics [24–26]. Periodic excitation of the supporting surface can produce rich responses including resonant amplification [27], period multiplication [28], intermittency [29], and chaotic attractors [30,31]. A large fraction of the established literature focuses on polygonal blocks or bodies with sharp features because their dynamics naturally involve impacts, switching constraints, and piecewise smooth flows [32–34]. In those settings, the origin of chaos is often traced to corner transitions [35], loss of contact [36], switch transitions [37], or restitution laws [38]. Smooth convex bodies are less frequently used as canonical examples for forced rocking chaos because they do not offer obvious

* Corresponding author.
E-mail address: dong.feng@rwth-aachen.de.

https://doi.org/10.1016/j.chaos.2026.118539
Received 9 February 2026; Received in revised form 20 April 2026; Accepted 15 May 2026
Available online 19 May 2026

discontinuities in geometry or kinematics, and their contact is often treated through local curvature approximations that reduce the geometric complexity [39,40].

Despite these advances, the case of a smooth near-spherical mono-monostatic body presents unresolved questions. For such bodies the restoring torques are entirely shape induced, and the identity of the active contact point is determined globally by which point on the surface attains the smallest height for the current attitude [41,42]. This introduces a nontrivial selection process that is distinct from the usual impact-driven mechanisms. However, modeling approaches either prescribe the contact along a simplified curve [43], or assume small angle approximations that suppress contact migration [44]. These simplifications limit the ability to capture how a mono-monostatic geometry can generate strong sensitivity to initial conditions under weak forcing, and they make it difficult to compare different analytical morphologies on equal footing.

The present work investigates forced rocking of homogeneous Gömböc bodies by embedding two analytical morphologies within a spherical radial surface representation and determining contact through a global height minimization of the rotated surface. This formulation naturally couples attitude dynamics to a contact selection mechanism that can switch between competing minimizing branches as parameters and states evolve. The study is motivated by the need for a physics-consistent benchmark model of smooth mono-monostatic bodies, where chaotic responses can arise from geometry-driven contact selection rather than impacts. The main objective is to quantify how morphology and forcing jointly govern contact-branch switching, attractor structure, and the onset of chaos, thereby providing guidance for exploiting self-righting shapes in vibration-driven transport and passive dynamic stabilization. The system is driven by biharmonic vertical excitation, which provides a controlled route to non-autonomous behavior while preserving a single contact constraint. The study then characterizes the resulting dynamics using stroboscopic Poincaré sampling and maximal Lyapunov exponents, and connects the onset of chaotic responses to separatrix splitting in a reduced near-saddle description. By comparing two analytical Gömböc morphologies with different phase functions, the work clarifies how morphology controls contact-branch structure and thereby shapes intermittency and crisis transitions in smooth convex body rocking.

2. Two analytical Gömböc morphologies and differential geometry of the surface

A body-fixed coordinate frame is attached to the center of mass. Spherical coordinates on the unit sphere are parameterized by colatitude ϕ and longitude θ, with $\phi \in (0,\pi)$ and $\theta \in [0,2\pi)$. The unit direction vector in the body frame is defined as:

$$\mathbf{u}(\phi,\theta) = \begin{bmatrix} \sin\phi\cos\theta \\ \sin\phi\sin\theta \\ \cos\phi \end{bmatrix}, \tag{1}$$

where the vector $\mathbf{u}$ has unit magnitude and specifies a ray from the center of mass.

A convex body surface is represented in spherical radial form by a scalar radius function $r(\phi,\theta)$ measured from the center of mass. The surface point in the body frame is:

$$\mathbf{x}(\phi,\theta) = r(\phi,\theta)\mathbf{u}(\phi,\theta), \tag{2}$$

where $\mathbf{x}$ is the position vector from the center of mass to a surface point.

Two analytical Gömböc morphologies are considered [45]. Both are specified through quartic relations for the radius and share a morphology parameter β. The symbol β is a dimensionless shape parameter that controls the amplitude of the radial modulation away from a sphere. For sufficiently small positive β, the shapes remain strictly convex.

The first morphology is defined by:

$$r(\phi,\theta)^4 = 1 + 4\beta\sin\phi\cos(\theta - 5\phi), \tag{3}$$

and its explicit radius function is:

$$r_1(\phi,\theta) = (1 + 4\beta\sin\phi\cos(\theta - 5\phi))^{\frac{1}{4}}. \tag{4}$$

The second morphology is defined by:

$$r(\phi,\theta)^4 = 1 + 4\beta\sin\phi\cos\left(\theta - \frac{3\pi}{2}\left(\cos\phi - \frac{\cos^3\phi}{3}\right)\right), \tag{5}$$

and its explicit radius function is:

$$r_2(\phi,\theta) = \left(1 + 4\beta\sin\phi\cos\left(\theta - \frac{3\pi}{2}\left(\cos\phi - \frac{\cos^3\phi}{3}\right)\right)\right)^{\frac{1}{4}}. \tag{6}$$

Both forms can be unified through a phase function $\chi(\phi,\theta)$ defined on the spherical parameter domain:

$$r(\phi,\theta) = (1 + 4\beta\sin\phi\cos\chi(\phi,\theta))^{\frac{1}{4}}. \tag{7}$$

For the first morphology the phase function is:

$$\chi_1(\phi,\theta) = \theta - 5\phi, \tag{8}$$

and for the second morphology the phase function is:

$$\chi_2(\phi,\theta) = \theta - \frac{3\pi}{2}\left(\cos\phi - \frac{\cos^3\phi}{3}\right). \tag{9}$$

The phase function χ controls the angular alignment of the radial modulation and is the primary distinction between the two analytical Gömböcs.

For differential geometric quantities, the derivatives of $\mathbf{u}$ are introduced:

$$\partial_\phi \mathbf{u} = \begin{bmatrix} \cos\phi\cos\theta \\ \cos\phi\sin\theta \\ -\sin\phi \end{bmatrix}, \partial_\theta \mathbf{u} = \begin{bmatrix} -\sin\phi\sin\theta \\ \sin\phi\cos\theta \\ 0 \end{bmatrix}. \tag{10}$$

These provide tangent directions on the unit sphere.

The auxiliary kernel $\mathscr{S}$ is introduced as a shorthand for the quartic expression inside the radius:

$$\mathscr{S}(\phi,\theta) = 1 + 4\beta\sin\phi\cos\chi(\phi,\theta). \tag{11}$$

The radius is then expressed compactly as:

$$r = \mathscr{S}^{\frac{1}{4}}. \tag{12}$$

The derivatives of the kernel are:

$$\partial_\phi \mathscr{S} = 4\beta\big(\cos\phi\cos\chi - \sin\phi\sin\chi\partial_\phi\chi\big), \partial_\theta \mathscr{S} = -4\beta\sin\phi\sin\chi\partial_\theta\chi. \tag{13}$$

The radius derivatives are:

$$\partial_\phi r = \frac{1}{4}\mathscr{S}^{-\frac{3}{4}}\partial_\phi \mathscr{S}, \partial_\theta r = \frac{1}{4}\mathscr{S}^{-\frac{3}{4}}\partial_\theta \mathscr{S}. \tag{14}$$

The surface tangents in the body frame are:

$$\partial_\phi \mathbf{x} = \big(\partial_\phi r\big)\mathbf{u} + r\partial_\phi \mathbf{u}, \partial_\theta \mathbf{x} = (\partial_\theta r)\mathbf{u} + r\partial_\theta \mathbf{u}. \tag{15}$$

The non-unit normal vector is defined as the cross product of tangents:

$$\mathbf{n}(\phi,\theta) = \partial_\phi \mathbf{x} \times \partial_\theta \mathbf{x}, \tag{16}$$

and the unit normal is:

$$\widehat{\mathbf{n}} = \frac{\mathbf{n}}{\|\mathbf{n}\|}. \tag{17}$$

The unit normal $\widehat{\mathbf{n}}$ will be used to express the contact condition in a coordinate-free manner.

The phase derivatives differ between the two morphologies. For the first morphology, they are:

$$\partial_\phi\chi_1 = -5, \partial_\theta\chi_1 = 1. \tag{18}$$

For the second morphology, they are:

$$\partial_\phi\chi_2 = -\frac{3\pi}{2}\left(\cos^2\phi\sin\phi - \sin\phi\right), \partial_\theta\chi_2 = 1. \tag{19}$$

The dependence of $\partial_\phi\chi_2$ on ϕ concentrates phase variation into specific latitude bands. This difference propagates into $\partial_\phi \mathscr{S}$, $\partial_\phi r$, and therefore into the distribution of local minima of the height functional introduced later.

3. Attitude kinematics and vertical excitation

The rigid-body attitude is represented by a rotation tensor $\mathbf{R}$ belonging to the special orthogonal group, and it maps vectors expressed in the body frame to vectors expressed in the inertial frame. The inertial vertical direction is denoted by the unit vector $\mathbf{e}_z$:

$$\mathbf{e}_z = \begin{bmatrix} 0 \\ 0 \\ 1 \end{bmatrix}. \tag{20}$$

The body-frame representation of the inertial vertical is denoted by $\mathbf{z}_b$ and is defined by:

$$\mathbf{z}_b = \mathbf{R}^{\mathrm{T}}\mathbf{e}_z, \tag{21}$$

where the vector $\mathbf{z}_b$ is the direction of the vertical in the body frame and changes in time as the body rocks.

Angular velocity expressed in the body frame is denoted by $\boldsymbol{\omega}$. The skew-symmetric tensor associated with a vector $\mathbf{a}$ is denoted by $[\mathbf{a}]_\times$ and satisfies $[\mathbf{a}]_\times \mathbf{b} = \mathbf{a} \times \mathbf{b}$ for any vector $\mathbf{b}$. Its matrix representation is:

$$[\mathbf{a}]_\times = \begin{bmatrix} 0 & -a_3 & a_2 \\ a_3 & 0 & -a_1 \\ -a_2 & a_1 & 0 \end{bmatrix}. \tag{22}$$

The attitude kinematics are then:

$$\dot{\mathbf{R}} = \mathbf{R}[\boldsymbol{\omega}]_\times. \tag{23}$$

This equation is the rigid-body kinematic relation in body angular velocity form.

A useful consequence is the evolution equation for $\mathbf{z}_b$. Differentiating $\mathbf{z}_b = \mathbf{R}^{\mathrm{T}}\mathbf{e}_z$ yields:

$$\dot{\mathbf{z}}_b = -\boldsymbol{\omega} \times \mathbf{z}_b. \tag{24}$$

The support undergoes prescribed vertical excitation, which is expressed through an effective gravitational acceleration $g_{eff}(t)$. The constant g is the gravitational acceleration. The excitation parameters are a_1 and a_2, the acceleration amplitudes of the fundamental and second harmonics; ω, the forcing angular frequency; and ψ, the phase shift of the second harmonic relative to the first. The effective gravity is:

$$g_{eff}(t) = g + a_1 \cos(\omega t) + a_2 \cos(2\omega t + \psi). \tag{25}$$

The time derivative of g_{eff} is:

$$\dot{g}_{eff}(t) = -a_1 \omega \sin(\omega t) - 2a_2 \omega \sin(2\omega t + \psi). \tag{26}$$

This explicit time dependence makes the dynamics non-autonomous and introduces parametric excitation of the restoring torques.

4. Contact selection by global height minimization and switching structure

The body is assumed to interact with a horizontal plane through a single point contact. For a strictly convex surface, a unique global minimizer exists for almost all attitudes, but near attitudes where two local minima have nearly equal height, the identity of the global minimizer can switch. This switching is central to the chaos mechanism discussed in this paper.

For a given attitude $\mathbf{R}$, the inertial height of a surface point $\mathbf{x}(\phi, \theta)$ is defined as the vertical component of the rotated point. The height functional is:

$$h(\phi, \theta; \mathbf{R}) = \mathbf{e}_z^{\mathrm{T}} \mathbf{R} \mathbf{x}(\phi, \theta). \tag{27}$$

Using $\mathbf{z}_b = \mathbf{R}^{\mathrm{T}}\mathbf{e}_z$, this can be written purely in body-frame quantities:

$$h(\phi, \theta; \mathbf{R}) = \mathbf{z}_b^{\mathrm{T}} \mathbf{x}(\phi, \theta). \tag{28}$$

The global contact parameters (ϕ^*, θ^*) are defined as the minimizer of h:

$$(\phi^*, \theta^*) = \operatorname*{argmin}_{\phi,\theta} h(\phi, \theta; \mathbf{R}). \tag{29}$$

The corresponding body-frame contact vector from the center of mass to the contact point is:

$$\mathbf{r}_c(\mathbf{R}) = \mathbf{x}(\phi^*, \theta^*), \tag{30}$$

where the vector $\mathbf{r}_c$ is a function of the attitude through the minimization process and constitutes a geometric nonlinearity.

Necessary conditions for an interior minimizer are the stationarity of h with respect to ϕ and θ:

$$\partial_\phi h(\phi^*, \theta^*; \mathbf{R}) = 0, \partial_\theta h(\phi^*, \theta^*; \mathbf{R}) = 0. \tag{31}$$

Using the derivatives of $\mathbf{x}$, these stationarity conditions are:

$$\mathbf{z}_b^{\mathrm{T}} \partial_\phi \mathbf{x}(\phi^*, \theta^*) = 0, \mathbf{z}_b^{\mathrm{T}} \partial_\theta \mathbf{x}(\phi^*, \theta^*) = 0. \tag{32}$$

Geometrically, these conditions imply that $\mathbf{z}_b$ is orthogonal to the tangent plane at the contact, hence parallel to the normal. This is expressed by:

$$\mathbf{z}_b \times \widehat{\mathbf{n}}(\phi^*, \theta^*) = \mathbf{0}. \tag{33}$$

Sufficient conditions for the minimizer to be a local minimum can be expressed using the Hessian of h on the parameter domain. The Hessian entries are defined as:

$$H_{\phi\phi} = \partial_{\phi\phi} h, H_{\phi\theta} = \partial_{\phi\theta} h, H_{\theta\theta} = \partial_{\theta\theta} h. \tag{34}$$

A sufficient condition for strict local minimality is:

$$H_{\phi\phi}(\phi^*,\theta^*) > 0, H_{\phi\phi}H_{\theta\theta} - H_{\phi\theta}^2 > 0. \tag{35}$$

The minimized height is:

$$h^*(\mathbf{R}) = \min_{\phi,\theta} h(\phi,\theta;\mathbf{R}). \tag{36}$$

The center of mass height above the plane is denoted by $\zeta(\mathbf{R})$ and is defined by:

$$\zeta(\mathbf{R}) = -h^*(\mathbf{R}). \tag{37}$$

This definition is consistent with the plane being tangent at the contact point so that the lowest surface point touches the plane.

When multiple local minima exist, the global minimizer can switch. Let $h_A(\mathbf{R})$ and $h_B(\mathbf{R})$ be two competing local minima values of the height functional. The switching surface in attitude space is characterized by equality of these branches:

$$h_A(\mathbf{R}) = h_B(\mathbf{R}). \tag{38}$$

Define the branch gap function $\Delta h(\mathbf{R})$ as:

$$\Delta h(\mathbf{R}) = h_A(\mathbf{R}) - h_B(\mathbf{R}). \tag{39}$$

Then, the switching occurs on the set $\Delta h(\mathbf{R}) = 0$. On one side of this set, the contact is associated with branch A, and on the other side it is associated with branch B. This yields a deterministic switching mechanism that can create large sensitivity to initial conditions under periodic forcing.

5. Equations of motion about the contact point and energy relations

The rigid body has mass m. The inertia tensor about the center of mass expressed in the body frame is denoted by the second-order tensor $\mathbf{I}_C$. The inertia tensor about the instantaneous contact point is denoted by $\mathbf{I}_P$ and is obtained via the parallel-axis theorem. The parallel-axis relation uses the contact vector $\mathbf{r}_c$ and its skew tensor:

$$\mathbf{I}_P(\mathbf{R}) = \mathbf{I}_C - m[\mathbf{r}_c]_\times[\mathbf{r}_c]_\times, \tag{40}$$

where the dependence on $\mathbf{R}$ is inherited through $\mathbf{r}_c(\mathbf{R})$.

The gravitational torque about the contact point is computed using the effective gravity $g_{eff}(t)$. The torque is denoted by $\boldsymbol{\tau}_g$ and is given by:

$$\boldsymbol{\tau}_g(\mathbf{R},t) = m g_{eff}(t)\mathbf{r}_c(\mathbf{R}) \times \mathbf{z}_b. \tag{41}$$

A linear rotational damping torque $\boldsymbol{\tau}_d$ is introduced to represent dissipative losses and is defined by a damping coefficient c:

$$\boldsymbol{\tau}_d = -c\boldsymbol{\omega}. \tag{42}$$

The total torque is:

$$\boldsymbol{\tau} = \boldsymbol{\tau}_g + \boldsymbol{\tau}_d. \tag{43}$$

Euler's equation about the contact point is:

$$\mathbf{I}_P(\mathbf{R})\dot{\boldsymbol{\omega}} + \dot{\mathbf{I}}_P(\mathbf{R},\dot{\mathbf{R}})\boldsymbol{\omega} + \boldsymbol{\omega} \times (\mathbf{I}_P(\mathbf{R})\boldsymbol{\omega}) = \boldsymbol{\tau}(\mathbf{R},\boldsymbol{\omega},t), \tag{44}$$

where $\dot{\mathbf{I}}_P$ is:

$$\dot{\mathbf{I}}_P = -m\left([\dot{\mathbf{r}}_c]_\times[\mathbf{r}_c]_\times + [\mathbf{r}_c]_\times[\dot{\mathbf{r}}_c]_\times\right). \tag{45}$$

Here, $\dot{\mathbf{r}}_c$ is the time derivative of the selected contact vector $\mathbf{r}_c(\mathbf{R})$, which exists whenever the active minimizer branch is unchanged. At contact-branch switching events, $\mathbf{r}_c$ changes discontinuously, and the model should be interpreted in a piecewise-smooth sense between switching instants.

Eq. (44) is coupled to the kinematic equation $\dot{\mathbf{R}} = \mathbf{R}[\boldsymbol{\omega}]_\times$ and to the contact selection map $\mathbf{r}_c(\mathbf{R})$. The full model therefore forms a non-autonomous system with state-dependent switching.

The kinetic energy about the contact point is defined as:

$$T(\mathbf{R},\boldsymbol{\omega}) = \frac{1}{2}\boldsymbol{\omega}^{\mathrm{T}}\mathbf{I}_P(\mathbf{R})\boldsymbol{\omega}. \tag{46}$$

The potential energy is defined using the center-of-mass height $\zeta(\mathbf{R})$ and the effective gravity:

$$V(\mathbf{R},t) = m g_{eff}(t)\zeta(\mathbf{R}). \tag{47}$$

The total energy is:

$$E(\mathbf{R},\boldsymbol{\omega},t) = T(\mathbf{R},\boldsymbol{\omega}) + V(\mathbf{R},t). \tag{48}$$

The instantaneous power input by torque is:

$$\mathscr{P} = \boldsymbol{\omega}^{\mathrm{T}}\boldsymbol{\tau}. \tag{49}$$

The dissipation power is:

$$\mathscr{P}_d = \boldsymbol{\omega}^{\mathrm{T}}\boldsymbol{\tau}_d = -c\|\boldsymbol{\omega}\|^2. \tag{50}$$

The gravitational power is:

$$\mathscr{P}_g = \boldsymbol{\omega}^{\mathrm{T}}\boldsymbol{\tau}_g. \tag{51}$$

These relations clarify the energetic roles of forcing and damping. Even in the absence of explicit impacts, the energy exchange can be strongly irregular because contact switching changes $\mathbf{r}_c$ and therefore changes $\mathbf{I}_P$ and $\boldsymbol{\tau}_g$ non-smoothly in time.

Finally, to make the formulation self-contained, the complete coupled model used throughout the paper is summarized here. The state variables are the attitude tensor $\mathbf{R}(t)$ and the body-frame angular velocity $\boldsymbol{\omega}(t)$. The geometry enters through the analytical surface map $\mathbf{x}(\phi,\theta)$ and the contact-selection rule, which defines the instantaneous contact vector $\mathbf{r}_c(\mathbf{R})$ via global height minimization. The external forcing enters only through the effective gravity $g_{\mathrm{eff}}(t)$. With these definitions, the governing dynamics form a non-autonomous rigid-body system with state-dependent contact selection:

$$\begin{cases} \mathbf{x}(\phi,\theta) = r(\phi,\theta)\mathbf{u}(\phi,\theta), \\ h(\phi,\theta;\mathbf{R}) = \mathbf{e}_z^{\mathrm{T}}\mathbf{R}\mathbf{x}(\phi,\theta), \\ (\phi^*,\theta^*) = \underset{\phi,\theta}{\operatorname{argmin}} h(\phi,\theta;\mathbf{R}), \\ \mathbf{r}_c(\mathbf{R}) = \mathbf{x}(\phi^*,\theta^*), \\ g_{\mathrm{eff}} = g + a_1\cos(\omega t) + a_2\cos(2\omega t + \psi), \\ \mathbf{z}_b = \mathbf{R}^{\mathrm{T}}\mathbf{e}_z, \\ \dot{\mathbf{R}} = \mathbf{R}[\boldsymbol{\omega}]_\times, \\ \mathbf{I}_P(\mathbf{R}) = \mathbf{I}_C - m[\mathbf{r}_c(\mathbf{R})]_\times[\mathbf{r}_c(\mathbf{R})]_\times, \\ \dot{\mathbf{I}}_P = -m\left([\dot{\mathbf{r}}_c]_\times[\mathbf{r}_c]_\times + [\mathbf{r}_c]_\times[\dot{\mathbf{r}}_c]_\times\right), \\ \boldsymbol{\tau}_g(\mathbf{R},t) = mg_{\mathrm{eff}}(t)\mathbf{r}_c(\mathbf{R}) \times \mathbf{z}_b, \\ \boldsymbol{\tau}_d = -c\boldsymbol{\omega}, \\ \boldsymbol{\tau} = \boldsymbol{\tau}_g + \boldsymbol{\tau}_d, \\ \mathbf{I}_P(\mathbf{R})\dot{\boldsymbol{\omega}} + \dot{\mathbf{I}}_P(\mathbf{R},\dot{\mathbf{R}})\boldsymbol{\omega} + \boldsymbol{\omega} \times (\mathbf{I}_P(\mathbf{R})\boldsymbol{\omega}) = \boldsymbol{\tau}(\mathbf{R},\boldsymbol{\omega},t). \end{cases} \tag{52}$$

In this system, contact switching occurs when the global minimizer changes between competing local minima of the height functional, which is detected by changes in (ϕ^*,θ^*) or equivalently by discontinuous changes in $\mathbf{r}_c(\mathbf{R})$. This summary provides a single reference for the coupled geometry, forcing, kinematics, and dynamics that are elaborated in the subsequent sections.

6. Nondimensional form, contact sensitivity, and chaos diagnostics

A nondimensionalization is introduced to identify essential parameter groups and to support efficient numerical exploration. A characteristic length scale L is defined as the spherical average of the radius function:

$$L = \frac{1}{4\pi}\int_0^{2\pi}\int_0^{\pi} r(\phi,\theta)\sin\phi\,\mathrm{d}\phi\,\mathrm{d}\theta. \tag{53}$$

The nondimensional time is:

$$\tau = \omega t. \tag{54}$$

The nondimensional angular velocity is:

$$\boldsymbol{\Omega} = \frac{\boldsymbol{\omega}}{\omega}. \tag{55}$$

The contact vector is nondimensionalized as:

$$\mathbf{p}_c = \frac{\mathbf{r}_c}{L}. \tag{56}$$

The inertia tensors are nondimensionalized by mL^2. The nondimensional inertia about the center of mass is $\mathbf{J}_C$ and that about the contact point is $\mathbf{J}_P$:

$$\mathbf{J}_C = \frac{\mathbf{I}_C}{mL^2}, \mathbf{J}_P = \frac{\mathbf{I}_P}{mL^2}. \tag{57}$$

Using the parallel-axis relation, there is:

$$\mathbf{J}_P = \mathbf{J}_C - [\mathbf{p}_c]_\times [\mathbf{p}_c]_\times. \tag{58}$$

A nondimensional damping coefficient γ is defined by:

$$\gamma = \frac{c}{mL^2\omega}. \tag{59}$$

A nondimensional gravity parameter κ is defined by:

$$\kappa = \frac{g}{L\omega^2}. \tag{60}$$

The forcing amplitudes are nondimensionalized by g to define A_1 and A_2:

$$A_1 = \frac{a_1}{g}, A_2 = \frac{a_2}{g}. \tag{61}$$

The normalized effective gravity becomes:

$$\frac{g_{eff}}{g} = 1 + A_1\cos\tau + A_2\cos(2\tau + \psi). \tag{62}$$

A nondimensional torque $\mathbf{\Gamma}$ is defined as $\mathbf{\Gamma} = \boldsymbol{\tau}/(mL^2\omega^2)$. Then, the nondimensional gravity torque and damping torque are:

$$\mathbf{\Gamma}_g = \kappa(1 + A_1\cos\tau + A_2\cos(2\tau + \psi))\mathbf{p}_c \times \mathbf{z}_b, \mathbf{\Gamma}_d = -\gamma\mathbf{\Omega}. \tag{63}$$

The nondimensional Euler equation reads:

$$\mathbf{J}_P\mathbf{\Omega}' + \mathbf{\Omega} \times (\mathbf{J}_P\mathbf{\Omega}) = \mathbf{\Gamma}_g + \mathbf{\Gamma}_d. \tag{64}$$

The nondimensional kinematics are:

$$\mathbf{R}' = \mathbf{R}[\mathbf{\Omega}]_\times. \tag{65}$$

The resulting parameter set consists of β, κ, γ, A_1, A_2, and ψ, together with the choice of phase function χ_1 or χ_2. To connect morphology to dynamics, sensitivity relations with respect to β are introduced. The derivative of the radius with respect to β is:

$$\frac{\partial r}{\partial \beta} = \frac{\sin\phi\cos\chi}{\mathscr{S}^{\frac{3}{4}}}. \tag{66}$$

The derivative of the surface point with respect to β is:

$$\frac{\partial \mathbf{x}}{\partial \beta} = \frac{\partial r}{\partial \beta}\mathbf{u}. \tag{67}$$

For a fixed attitude, the derivative of the height functional with respect to β is:

$$\frac{\partial h}{\partial \beta} = \mathbf{z}_b^{\mathrm{T}}\frac{\partial \mathbf{x}}{\partial \beta}. \tag{68}$$

When the minimizer is unique and varies smoothly with β, the sensitivity of the minimized height can be approximated by the derivative evaluated at the minimizer:

$$\frac{\partial h^*}{\partial \beta} \approx \left.\frac{\partial h}{\partial \beta}\right|_{(\phi^*,\theta^*)}. \tag{69}$$

This expression makes explicit how β shifts the effective potential and therefore alters the proximity to separatrix structures that underlie chaotic transitions.

Contact sensitivity to attitude can be formalized by defining the stationarity functions:

$$F_1(\phi, \theta; \mathbf{R}) = \mathbf{z}_b^{\mathrm{T}}\partial_\phi \mathbf{x}, F_2(\phi, \theta; \mathbf{R}) = \mathbf{z}_b^{\mathrm{T}}\partial_\theta \mathbf{x}. \tag{70}$$

At contact, the following conditions hold:

$$F_1(\phi^*, \theta^*; \mathbf{R}) = 0, F_2(\phi^*, \theta^*; \mathbf{R}) = 0. \tag{71}$$

Linearizing these conditions yields an implicit relation between attitude perturbations and changes in (ϕ^*, θ^*):

$$\begin{bmatrix} \partial_\phi F_1 & \partial_\theta F_1 \\ \partial_\phi F_2 & \partial_\theta F_2 \end{bmatrix} \begin{bmatrix} \delta\phi^* \\ \delta\theta^* \end{bmatrix} = -\begin{bmatrix} \delta F_1 \\ \delta F_2 \end{bmatrix}. \tag{72}$$

When the matrix on the left is invertible, the minimizer is locally well-defined. Near switching sets, the invertibility may degrade due to competing branches, which supports the interpretation of switching as a geometric source of sensitive dependence.

Chaos diagnostics are formulated in terms of stroboscopic sampling and Lyapunov exponents. The forcing period T is defined by $T = 2\pi/\omega$. The stroboscopic map $\mathscr{P}$ is defined by integrating the flow over one period:

$$\mathbf{y}_{n+1} = \mathscr{P}(\mathbf{y}_n). \tag{73}$$

where state $\mathbf{y}$ collects the attitude and angular velocity, $\mathbf{y} = (\mathbf{R}, \boldsymbol{\Omega})$. Sampling times are:

$$t_n = t_0 + nT. \tag{74}$$

A Poincaré set is obtained from sampled angular velocities $\{\boldsymbol{\Omega}(t_n)\}$ after discarding transients.

Lyapunov exponents are defined through the evolution of an infinitesimal perturbation $\delta\mathbf{y}$ governed by the variational equation:

$$\frac{\mathrm{d}}{\mathrm{d}t}\delta\mathbf{y} = \mathbf{A}(t)\delta\mathbf{y}. \tag{75}$$

where $\mathbf{A}(t)$ is the Jacobian tensor of the vector field with respect to the state, and it is generally time-dependent due to $g_{eff}(t)$ and branch-dependent due to contact switching. The maximal Lyapunov exponent is [46]:

$$\lambda_{max} = \lim_{t\to\infty}\frac{1}{t}\ln\frac{\|\delta\mathbf{y}(t)\|}{\|\delta\mathbf{y}(0)\|}. \tag{76}$$

A practical period-wise estimator with renormalization uses separations δ_n at times t_n and a fixed reset size δ_0:

$$\lambda_{max} \approx \frac{1}{NT}\sum_{n=1}^{N}\ln\frac{\delta_n}{\delta_0}. \tag{77}$$

A positive value of λ_{max} indicates sensitive dependence and supports the presence of a strange attractor in the stroboscopic dynamics.

7. Reduced separatrix-splitting analysis and morphology-dependent thresholds

To connect forcing parameters to a chaos onset criterion, a reduced near-saddle model is introduced. The unstable equilibrium corresponds to a saddle of an effective potential. A generalized coordinate q describes rocking motion along a dominant direction, and p denotes its conjugate momentum. The reduced conservative dynamics are expressed in Hamiltonian form:

$$\dot{q} = \frac{\partial H_0}{\partial p}, \dot{p} = -\frac{\partial H_0}{\partial q}. \tag{78}$$

The conservative Hamiltonian is written as:

$$H_0(q,p) = \frac{p^2}{2M(q)} + U(q), \tag{79}$$

where the function $M(q)$ is an effective mass and satisfies:

$$M(q) > 0. \tag{80}$$

The potential $U(q)$ has a saddle at $q = q_u$:

$$U'(q_u) = 0, U''(q_u) < 0. \tag{81}$$

The separatrix energy is:

$$E_s = U(q_u). \tag{82}$$

A homoclinic orbit on the separatrix is denoted by $q_h(t)$ and satisfies:

$$H_0(q_h(t), p_h(t)) = E_s, p_h(t) = M(q_h(t))\dot{q}_h(t). \tag{83}$$

Damping and biharmonic excitation are introduced as a small perturbation with strength ε. The biharmonic form is important here because it offers two independent control knobs, the second-harmonic amplitude and the phase shift, which allow the separatrix-splitting condition and the resulting basin structure to be tuned without changing the primary forcing frequency. Moreover, the second harmonic generically breaks simple single-frequency symmetry and enhances effective stretching and folding in the stroboscopic dynamics, thereby widening the parameter window where robust chaotic responses can be observed and compared across morphologies. Then, the perturbed system is:

$$\dot{q} = \frac{\partial H_0}{\partial p}, \dot{p} = -\frac{\partial H_0}{\partial q} + \varepsilon G(q,p,t). \tag{84}$$

A representative perturbation compatible with damping and biharmonic forcing is:

$$G(q,p,t) = -\mu p + \nu_1 S(q)\cos(\omega t) + \nu_2 S(q)\cos(2\omega t + \psi), \tag{85}$$

where μ is a damping parameter, ν_1 and ν_2 are forcing coefficients, and $S(q)$ represents the coupling of vertical excitation to the reduced coordinate.

The Melnikov analysis in this section is intended as a reduced, near-separatrix indicator rather than as a fully rigorous theorem for the complete three-dimensional contact-selection dynamics [47]. The full Gömböc system is non-autonomous and becomes piecewise smooth because the contact vector $\mathbf{r}_c(\mathbf{R})$ can change discontinuously when the global height minimizer switches between competing local minima. Consequently, the exact flow may include switching instants at which derivatives with respect to the state are not classically defined. For this reason, the Melnikov method is applied only to an idealized reduced subsystem that captures the dominant near-saddle rocking direction on a fixed contact-selection branch, where the effective restoring behavior can be represented by a smooth scalar potential.

Within this reduced setting, the unperturbed dynamics are assumed to be a smooth one-degree-of-freedom Hamiltonian system of the form given in Eqs. (78)–(83), with a smooth effective mass $M(q)$ and a smooth effective potential $U(q)$. The existence of a saddle point of $U(q)$ implies the existence of a separatrix level set in the (q,p) phase plane, and the corresponding homoclinic orbit $q_h(t)$ is assumed to exist as the separatrix trajectory associated with the unstable equilibrium. This assumption is standard for smooth Hamiltonian systems with a single saddle in the effective potential and is used here to establish a reference separatrix geometry against which perturbation-induced manifold splitting is evaluated [47].

Regarding perturbation regularity, the forcing and damping terms used in $G(q,p,t)$ are smooth in time and smooth in (q,p) for any smooth coupling function $S(q)$. The small perturbation requirement is interpreted in the conventional Melnikov sense as a scale separation in which the combined damping and excitation are weak relative to the characteristic near-separatrix energy scale of the reduced Hamiltonian, so that the perturbed stable and unstable manifolds remain close to the unperturbed separatrix over one passage. Under this assumption, the Melnikov function provides a leading-order approximation for the distance between invariant manifolds in the reduced system, and a sign-changing Melnikov function yields a sufficient indicator for transverse intersections and the associated Smale-type dynamics in the reduced model.

Finally, because the complete Gömböc dynamics include geometry-driven contact selection and possible switching between minimizing branches, the Melnikov criterion is used in this work as a qualitative link between forcing parameters, morphology-dependent effective potentials, and the onset of complex responses, rather than as a stand-alone proof of chaos for the full system. The main conclusions regarding chaotic behavior are therefore supported independently by direct numerical diagnostics of the full model, including Poincaré sampling, return-map structure, and maximal Lyapunov exponent estimates.

The Melnikov function is introduced to measure the first-order distance between the perturbed stable and unstable manifolds in the reduced phase space [48]. It is defined by:

$$\mathcal{M}(t_0) = \int_{-\infty}^{\infty} p_h(t) G(q_h(t), p_h(t), t + t_0)\mathrm{d}t. \tag{86}$$

Substituting G yields:

$$\mathcal{M}(t_0) = -\mu \int_{-\infty}^{\infty} p_h(t)^2 \mathrm{d}t + \nu_1 \int_{-\infty}^{\infty} p_h(t) S(q_h(t))\cos(\omega(t+t_0))\mathrm{d}t + \nu_2 \int_{-\infty}^{\infty} p_h(t) S(q_h(t))\cos(2\omega(t+t_0)+\psi)\mathrm{d}t. \tag{87}$$

Define the dissipative integral:

$$D = \int_{-\infty}^{\infty} p_h(t)^2 \mathrm{d}t. \tag{88}$$

Define Fourier-type response integrals for the fundamental harmonic:

$$C_1 = \int_{-\infty}^{\infty} p_h(t) S(q_h(t))\cos(\omega t)\mathrm{d}t, S_1 = \int_{-\infty}^{\infty} p_h(t) S(q_h(t))\sin(\omega t)\mathrm{d}t. \tag{89}$$

and for the second harmonic:

$$C_2 = \int_{-\infty}^{\infty} p_h(t) S(q_h(t))\cos(2\omega t)\mathrm{d}t,$$

$$S_2 = \int_{-\infty}^{\infty} p_h(t) S(q_h(t))\sin(2\omega t)\mathrm{d}t. \tag{90}$$

The Melnikov function can then be expressed as:

$$\mathcal{M}(t_0) = -\mu D + \nu_1(C_1\cos(\omega t_0) - S_1\sin(\omega t_0)) + \nu_2(C_2\cos(2\omega t_0+\psi) - S_2\sin(2\omega t_0+\psi)). \tag{91}$$

Define the harmonic amplitudes:

$$A_1^* = \sqrt{C_1^2 + S_1^2}, A_2^* = \sqrt{C_2^2 + S_2^2}. \tag{92}$$

A sufficient criterion for transverse intersection of manifolds, and therefore for the possibility of chaotic dynamics in the reduced system, is that the forcing terms exceed the dissipative term in magnitude:

$$\nu_1 A_1^* + \nu_2 A_2^* > \mu D. \tag{93}$$

In the Gömböc setting, the functions $U(q)$, $M(q)$, and $S(q)$ depend implicitly on the morphology and on the contact selection map. Consequently, the integrals D, A_1^*, and A_2^* depend on the phase function χ and on β. This provides a mechanism by which the two analytical Gömböcs can exhibit different chaos thresholds and different crisis patterns even under identical forcing parameters.

8. Results

Based on the parameter settings in Table 1, a series of numerical experiments were conducted to validate the effectiveness of the analytical framework in this study. Two analytical Gömböc morphologies were examined under identical forcing and dissipation conditions in order to isolate the influence of shape on contact selection and long-time dynamics. For each morphology, the surface was discretized at a fixed resolution to enable efficient global contact identification via height minimization at every time step, and the resulting rigid-body equations were integrated with a fixed-step fourth-order scheme to ensure consistent phase accuracy across long integrations. Baseline simulations were first performed to characterize the temporal evolution of angular velocity, minimized height, an energy proxy, and switching activity, which together provide a direct view of how contact branch changes modulate the response. The same baseline runs were then analyzed using stroboscopic sampling and return maps to reveal invariant set structure, complemented by spectral content and phase portraits to distinguish broadband responses from nearly periodic motion. Chaotic behavior was further assessed through maximal Lyapunov exponent estimates computed from nearby trajectories and summarized both as a single scalar indicator and as a time-evolving measure to expose transient growth and convergence. Finally, coarse parameter scans were carried out over forcing frequency and excitation amplitudes, as well as over the second harmonic amplitude and phase shift, to map regions of elevated response intensity and contact switching and to compare how the two morphologies organize these regions in parameter space.

For numerical implementation, the analytical surface $\mathrm{x}(\phi,\theta)$ is evaluated on a fixed tensor-product grid in the spherical parameter domain, using N_ϕ samples in colatitude and N_θ samples in azimuth as reported in Table 1. This produces a discrete set of body-frame surface points that remains fixed throughout a simulation, and all contact queries are performed on this precomputed point cloud.

At each time step, the current attitude $\mathbf{R}(t)$ obtained from integrating the kinematic equation is used to evaluate the height functional over all discrete surface points. The active contact is selected as the global minimizer of height within the discrete set, and the corresponding contact vector $\mathbf{r}_c(\mathbf{R})$ is updated accordingly. This update is performed at every integration step so that contact migration is fully coupled to the attitude evolution rather than prescribed a priori. Contact-branch switching occurs naturally when the identity of the global minimizer changes between consecutive steps, which is detected numerically as a change in the minimizing grid index and, equivalently, as a discontinuous update of $\mathbf{r}_c$.

Once $\mathbf{r}_c(\mathbf{R})$ is selected, the instantaneous inertia about the contact point is assembled using the parallel-axis relation, and the gravitational and damping torques are evaluated using the same contact vector and the current body-frame vertical $\mathbf{z}_b$. The angular-velocity equation is then advanced using the time-varying contact-point formulation in Eq. (44) together with the kinematics, forming a closed update cycle at each time step. Between switching instants the model is interpreted as smooth on a fixed minimizer branch, while switching produces a piecewise-smooth trajectory driven by discrete updates of the active minimizer. This explicit coupling strategy, which consists of precomputing the discretized surface, performing height minimization at each step, and then integrating the rigid-body dynamics using the selected contact, is the numerical model underlying all reported simulations and figures.

Table 1
Parameter settings.

Symbol	Meaning	Value
β	Morphology parameter in the radial function $r(\phi,\theta)$	0.12
N_ϕ	Number of colatitude grid points for contact minimization	90
N_θ	Number of longitude grid points for contact minimization	180
m	Mass	1
g	Gravitational acceleration	9.81
c	Linear rotational damping coefficient	0.02
ω	Forcing angular frequency	18.0
A_1	Fundamental vertical acceleration amplitude	2.0
A_2	Second-harmonic vertical acceleration amplitude	1.0
ψ	Phase shift of the second harmonic	$\pi/3$
stepsPerT	RK4 steps per forcing period, main run	160
N_{per}	Number of forcing periods, main run	300
δ_0	Initial perturbation magnitude for Lyapunov estimate	10^{-7}
$\boldsymbol{\omega}_0$	Initial angular velocity	$[0,0,0]^{\mathrm{T}}$

8.1. Dynamics and contact selection mechanism

Fig. 1 compares the two analytical Gömböc morphologies considered in this study through a three-dimensional surface rendering and a corresponding radial map on the spherical parameter domain. The surface is represented in spherical–radial form, where r denotes the distance from the center of mass to the surface along a direction specified by the spherical angles ϕ and θ. Here, ϕ is the colatitude ranging from 0 to π, and θ is the azimuth ranging from 0 to 2π. The color scale in the radial maps visualizes the magnitude of r, thereby highlighting how each shape deviates from a perfect sphere.

Both morphologies remain close to spherical, with r varying within a relatively narrow band, which is consistent with the intended near-spherical mono-monostatic character. This small yet structured variation is crucial: it is sufficiently weak to preserve convexity and smoothness, but sufficiently organized to induce a nontrivial distribution of low-height candidates that later govern contact selection under rotation. In the rendered surfaces, this manifests as subtle bulging and flattening rather than sharp features, indicating that the strong nonlinearity observed later does not rely on corners or impacts.

A clear distinction between the two morphologies emerges in the topology of the radial maps. For Gömböc I, the radius map exhibits nearly uniform, diagonally oriented banding across the (ϕ, θ) domain, suggesting an approximately constant phase winding with respect to ϕ. This structure implies that as the body rotates, comparable radial extrema are encountered in a relatively regular progression along latitude. In contrast, Gömböc II shows banding that is visibly distorted and unevenly distributed over ϕ, with broader regions of gradual variation and more concentrated regions of steeper gradients. This indicates that the radial modulation is redistributed toward specific latitude bands, which is expected to alter how many competing low-height candidates coexist for a given attitude.

From a dynamical perspective, the radial maps provide an immediate geometric explanation for why the two bodies can exhibit different contact-branch organizations under identical excitation conditions. The more uniform band structure of Gömböc I suggests smoother migration of the global height minimizer, whereas the latitude-dependent distortion visible in Gömböc II indicates a higher likelihood of localized competition among minima. This morphological difference is later reflected in differences in switching activity, attractor structure, and parameter-space response surfaces, even when the excitation parameters are held fixed.

Fig. 2 visualizes the contact selection mechanism through the height landscape evaluated over the spherical parameter domain for a representative attitude taken from the baseline simulation. The plotted scalar field is the surface height, defined as the vertical projection of the rotated surface point, and the white marker indicates the global minimizer that determines the instantaneous contact point. The two right-hand panels provide local zooms around the minimizer to reveal the curvature and anisotropy of the minimum basin, which are directly related to the local stability of the selected contact under small perturbations of attitude.

For Gömböc I, the height field exhibits a pronounced low-height basin embedded within a broader undulating landscape. The

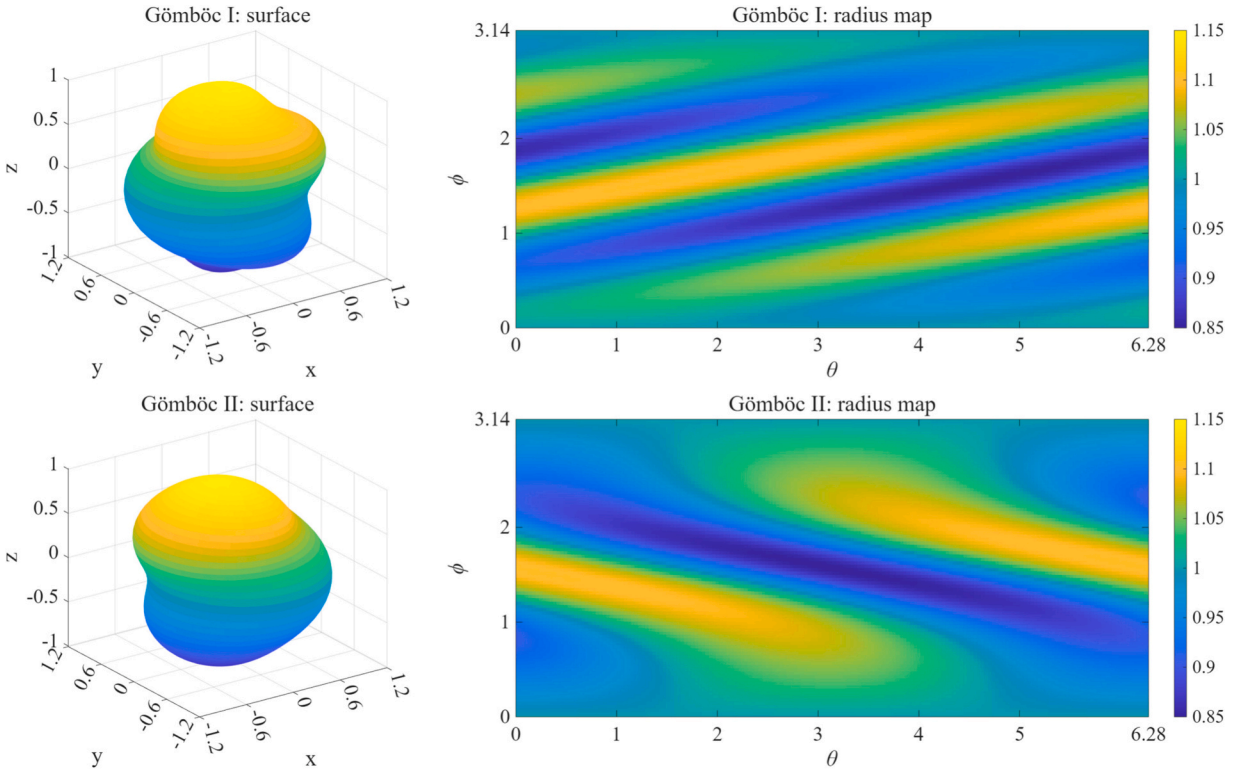

Fig. 1. Analytical Gömböc morphologies and radial maps.

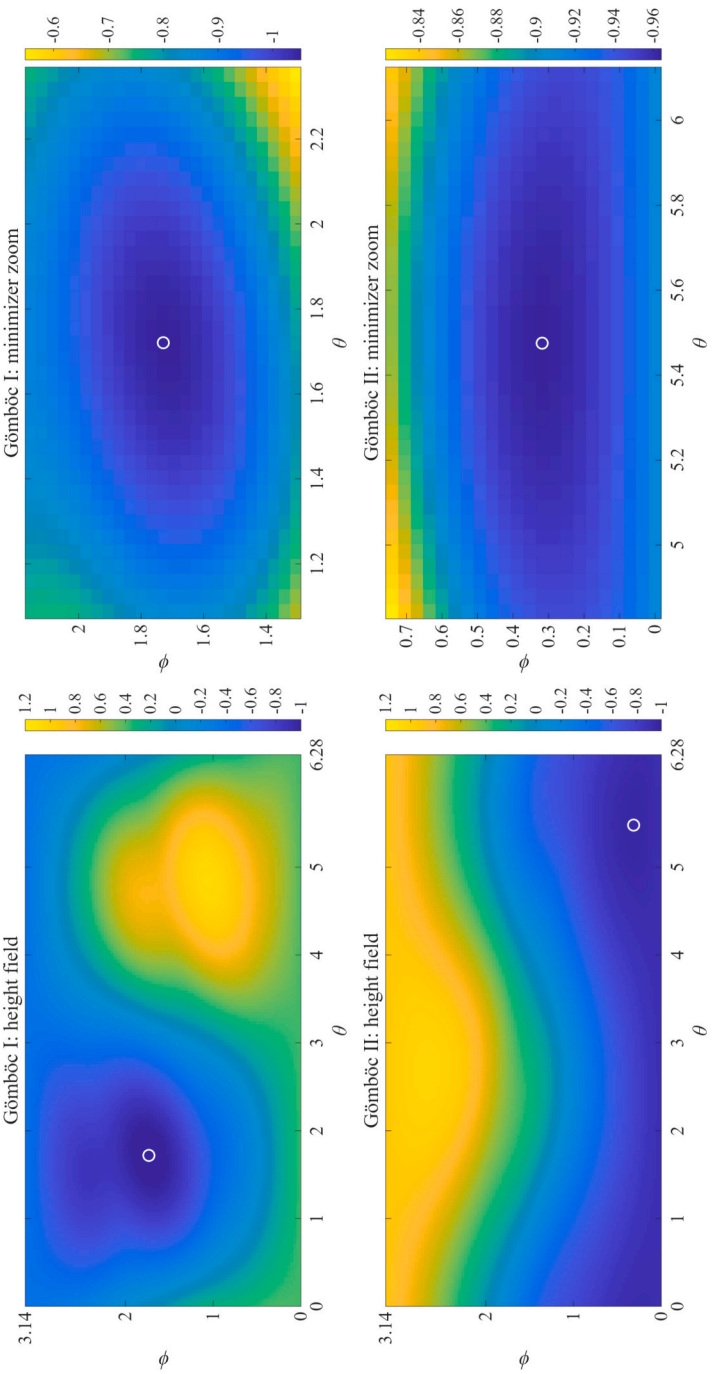

Fig. 2. Contact selection height landscapes and local minimizer structure.

minimizer lies inside a well-defined depression, while other regions of the domain attain substantially higher values, indicating strong geometric contrast between the active contact region and non-contact candidates. The zoomed panel shows that the minimum basin is elongated, implying direction-dependent sensitivity of the minimizing parameters. Such anisotropy is consistent with contact migration that can be smooth along one parameter direction yet more abrupt along the orthogonal direction when the attitude evolves, which later contributes to intermittent switching intensity under excitation.

For Gömböc II, the height field is organized differently under the same forcing conditions. The global minimum appears closer to the boundary of the displayed domain in the full field, and the overall landscape shows a stronger large-scale gradient across colatitude. The zoomed panel highlights a comparatively flatter minimum basin in the neighborhood of the minimizer, with weaker local variation than in Gömböc I. This indicates that a wider set of nearby surface points can remain competitive in height, which is a geometric precursor to branch competition. In practical terms, a flatter neighborhood increases the likelihood that small attitude changes or forcing-driven oscillations can alter the identity of the global minimizer, thereby enhancing contact selection switching activity.

Across both morphologies, the color ranges indicate that the active minima occur at negative height values of order unity in the chosen normalization, while surrounding regions can differ by a substantial fraction of the full scale. This contrast supports the interpretation that the contact is governed by a global selection rule rather than by a locally prescribed rolling curve. The qualitative differences between the two height landscapes in Fig. 2 provide an early geometric explanation for why the two analytical morphologies can exhibit distinct contact-branch structures and therefore distinct routes toward complex and chaotic responses in later diagnostics.

Fig. 3 summarizes the baseline response of the two analytical Gömböcs under identical excitation and dissipation parameters by reporting four time-domain observables over the first 100 s. The angular velocity components ω_x, ω_y, and ω_z characterize the instantaneous rocking and twisting dynamics in the body frame. The minimized height h^* denotes the minimum of the height functional over the surface at each time, and therefore tracks the currently selected contact branch through the global height minimization rule. The plotted energy quantity E is an energy proxy constructed from the instantaneous inertia about the active contact point and the effective gravity. Switching events are marked by dots on the energy time history, where a switch indicates a change in the identity of the minimizing surface point. The switching rate estimate is obtained from a moving average of the switch indicator and provides a coarse measure of contact selection activity in time.

For Gömböc I, the angular velocity components exhibit a mixture of irregular amplitude modulation and intervals of more structured oscillations. This behavior is consistent with non-autonomous forcing combined with geometry-driven contact selection, where the system alternates between regimes of relatively coherent rocking and regimes where multiple modes participate. The minimized height h^* shows repeated sharp excursions separated by segments of comparatively smoother oscillation. These excursions indicate episodes in which the global minimizer changes rapidly in response to the evolving attitude, implying intensified contact-branch competition. The energy proxy E remains bounded within a relatively narrow range while displaying dense fluctuations, confirming sustained forcing-dissipation balance without monotone drift. The distribution of switching markers is visibly nonuniform, and the switching-rate curve supports this interpretation by showing a pronounced temporal variation, including a mid-interval enhancement followed by a sustained reduction. This nonstationarity suggests that the trajectory explores distinct regions of the attitude-dependent contact landscape over the course of the run.

For Gömböc II, the angular velocity components show a more consistently structured oscillatory pattern, with frequent excursions and less pronounced long-term modulation than observed for Gömböc I. The minimized height h^* exhibits persistent spike-like events throughout the interval, indicating that rapid contact updates remain active over long times rather than being concentrated in a limited window. The energy proxy again remains bounded with dense fluctuations, but the switching markers appear more uniformly distributed in time. This is consistent with the switching-rate estimate, which stays elevated and relatively steady across the interval compared with the more variable behavior of Gömböc I. In combination with the height-landscape differences in Fig. 2, these observations support the conclusion that the second morphology sustains more persistent contact-branch competition under the same forcing conditions.

Overall, Fig. 3 provides time-domain evidence that morphology alters not only the amplitude statistics of $\boldsymbol{\omega}$ but also the temporal organization of contact selection, as reflected in h^* and switching-rate variability. These baseline signatures motivate the subsequent stroboscopic and Lyapunov diagnostics, where the same differences are recast in terms of attractor geometry and sensitivity to initial conditions.

Fig. 4 resolves the contact dynamics that underlie the baseline responses by reporting the evolution of the discrete contact index, a smoothed estimate of the switching rate, and the three components of the contact vector $\mathbf{r}_c$ in the body frame. The contact index is the integer label of the surface point that attains the global minimum of the height functional at each time step, as determined by the discrete surface representation used for contact selection. Although the index itself has no intrinsic geometric meaning, abrupt jumps in the index provide an unambiguous indicator of contact-branch changes. The contact coordinates $\mathbf{r}_c = \left(r_{c,x}, r_{c,y}, r_{c,z}\right)^{\mathrm{T}}$ are obtained by mapping the selected index back to the corresponding surface point in the precomputed point cloud, thereby providing a physically interpretable description of how the contact location migrates over the body.

For Gömböc I, the contact index shows clear episodes of intermittent behavior. Early in the record, the index exhibits repeated abrupt jumps interspersed with intervals of gradual drift, indicating alternating phases of rapid contact switching and smoother contact migration. A long interval of comparatively regular evolution is visible later, where the index varies more smoothly with a pronounced low-frequency trend. This transition is consistent with the switching-rate estimate, which rises to a higher level during the interval of dense jumps and then decreases markedly, remaining low for an extended time before partially recovering near the end of

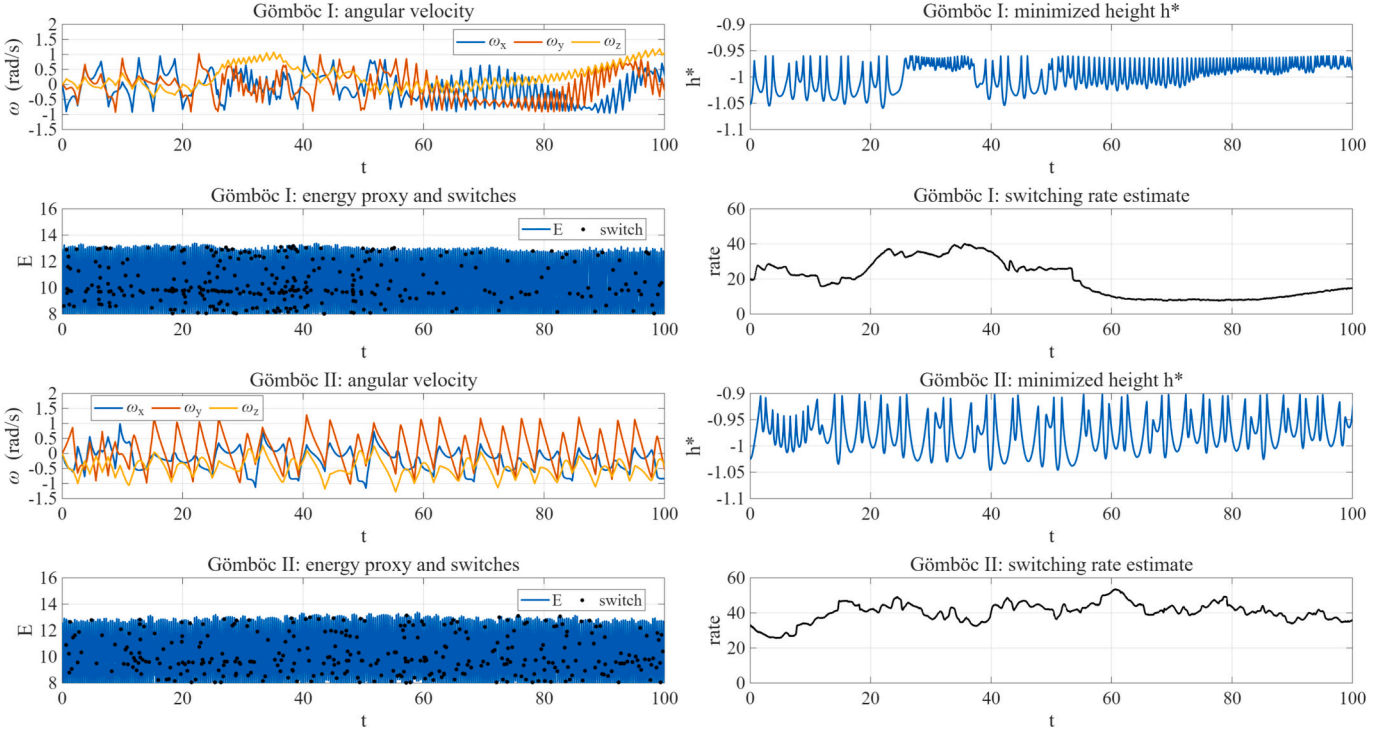

Fig. 3. Baseline time histories of angular velocity, minimized height, energy, and switching rate.

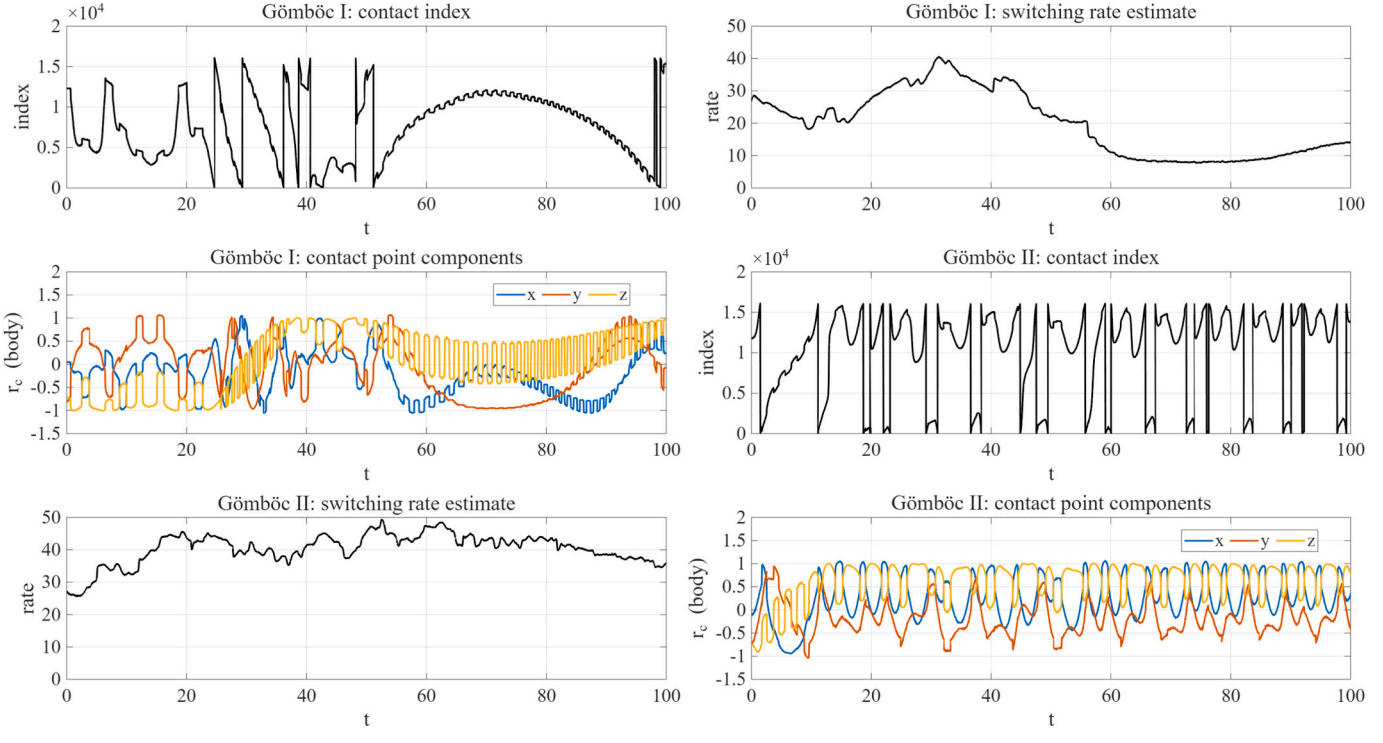

Fig. 4. Contact-point dynamics: index evolution, switching statistics, and contact coordinates.

the window. The contact-coordinate traces support this interpretation. During intervals of frequent switching, the components of $\mathbf{r}_c$ show rapid, piecewise changes, whereas during the smoother interval they become more coherent and exhibit nearly periodic modulation, especially in the vertical component $r_{c,z}$. This separation of regimes suggests that the trajectory alternates between regions of the attitude space where the global minimizer is well isolated and regions where multiple local minima are competitive.

For Gömböc II, the contact index is dominated by frequent discontinuous resets over the full time window. Compared with Gömböc I, the index time history shorter intervals of smooth drift and more persistent jump activity, which aligns with the elevated and comparatively steady switching-rate estimate. The contact coordinates exhibit a repeating, pulse-like pattern in the components, particularly in $r_{c,z}$, indicating recurrent excursions of the contact location between distinct regions of the surface. The persistence of this pattern supports the view that, for this morphology, the global minimizer remains in closer competition with alternative candidates over a wider portion of the trajectory, leading to sustained contact-branch switching under the same forcing conditions.

Overall, Fig. 4 clarifies that the complexity observed in the baseline time histories is not solely reflected in $\boldsymbol{\omega}$ or in the minimized height h^*, but is directly encoded in the geometry-driven evolution of the contact point itself. The contrast between intermittent switching in Gömböc I and sustained switching in Gömböc II provides a concrete morphology-dependent mechanism that later manifests in differences in Poincaré structure, spectral broadening, Lyapunov growth, and parameter-space response surfaces.

In addition to the biharmonic-forcing results, Fig. 5 and Fig. 6 report a harmonic-excitation benchmark obtained by keeping all baseline parameters unchanged while removing the second harmonic. In this case, the effective vertical acceleration is:

$$g_{\mathrm{eff}}(t) = g + A_1 \cos(\omega t), \tag{94}$$

so the response is driven by a single-frequency modulation of gravity with the same ω and A_1 as in the baseline setting (see Table 1), and with $A_2 = 0$.

The time histories show that both morphologies still sustain bounded, nontrivial motion over the 0–100 s window, but with morphology-dependent organization. For Gömböc I, the angular-velocity components exhibit a clear transition from a more irregular early-time regime to a later interval with stronger oscillatory regularity, accompanied by a gradual bias in the component amplitudes. The minimized height h^* remains within a narrow band and displays repeated sharp excursions that gradually become more regular after mid-time, consistent with the system entering a more organized contact-selection regime. The energy proxy remains bounded and densely fluctuating, indicating sustained exchange between forcing and dissipation without drift, while the switching-rate estimate is distinctly nonstationary, decreasing early, rising to a pronounced hump around the mid-interval, and then decaying again toward late times. For Gömböc II, the angular velocity appears more persistently oscillatory with less pronounced long-term modulation, and h^* shows sustained spike-like events across the entire interval. The switching-rate estimate for Gömböc II is comparatively steadier, remaining elevated with only moderate slow variation, consistent with persistent contact-branch competition even under purely harmonic excitation.

The contact-index traces provide direct evidence that the dominant nonlinearity under harmonic forcing still arises from geometry-driven contact selection. For Gömböc I, the index alternates between intervals of smooth drift and abrupt jumps, indicating intermittent switching between minimizing branches. These switching episodes align with the mid-interval increase in the switching-rate estimate. The contact coordinates $\mathbf{r}_c$ exhibit corresponding behavior: during high-switching intervals, the components change more abruptly and irregularly, whereas during lower-switching intervals they become more coherent and quasi-periodic, especially in the vertical component. For Gömböc II, the contact index shows frequent, repeated reset-like transitions throughout the time window, and the contact coordinates display a highly regular, pulse-like pattern, indicating repeated migration among a small set of preferred contact regions on the surface. This morphology therefore maintains a stronger tendency toward persistent branch competition under harmonic forcing, matching the steadier switching-rate estimate.

Overall, these two figures demonstrate that the absence of the second harmonic does not eliminate contact switching or complex dynamics, but it reshapes their temporal organization. Harmonic excitation tends to promote more coherent intervals for Gömböc I while Gömböc II retains sustained switching activity, supporting the interpretation that morphology controls how single-frequency parametric forcing organizes contact-branch competition and the resulting response regimes.

8.2. Attractor diagnostics and chaotic signatures

Fig. 7 reports stroboscopic diagnostics of the baseline responses through Poincaré sampling and one-step return maps. The Poincaré clouds are obtained by sampling the angular-velocity vector $\boldsymbol{\omega}$ once per forcing period after transients, yielding a discrete set in three-dimensional ω-space that reflects the invariant structure of the stroboscopic map. The one-step return maps plot $\omega_x(n+1)$ against $\omega_x(n)$, where n indexes successive Poincaré samples, and provide a compact view of correlation, stretching, and folding in the sampled dynamics.

For Gömböc I, the Poincaré cloud forms a broad, flattened distribution rather than a small set of isolated points. This indicates that the stroboscopic dynamics do not settle onto a simple periodic orbit over the observation window, but instead explore a higher-dimensional invariant set. The corresponding return map shows a widely scattered point set with an overall increasing trend, suggesting significant variability in $\omega_x(n+1)$ for a given $\omega_x(n)$. Such dispersion is consistent with sensitive dependence and the presence of nonlinear stretching and folding mechanisms, which in the present setting are induced by the combination of biharmonic excitation and contact selection switching.

For Gömböc II, the Poincaré cloud is also extended, but appears more concentrated along a tilted manifold-like region compared with Gömböc I. The return map reveals a clearer banded structure with clusters aligned along an increasing relation, indicating

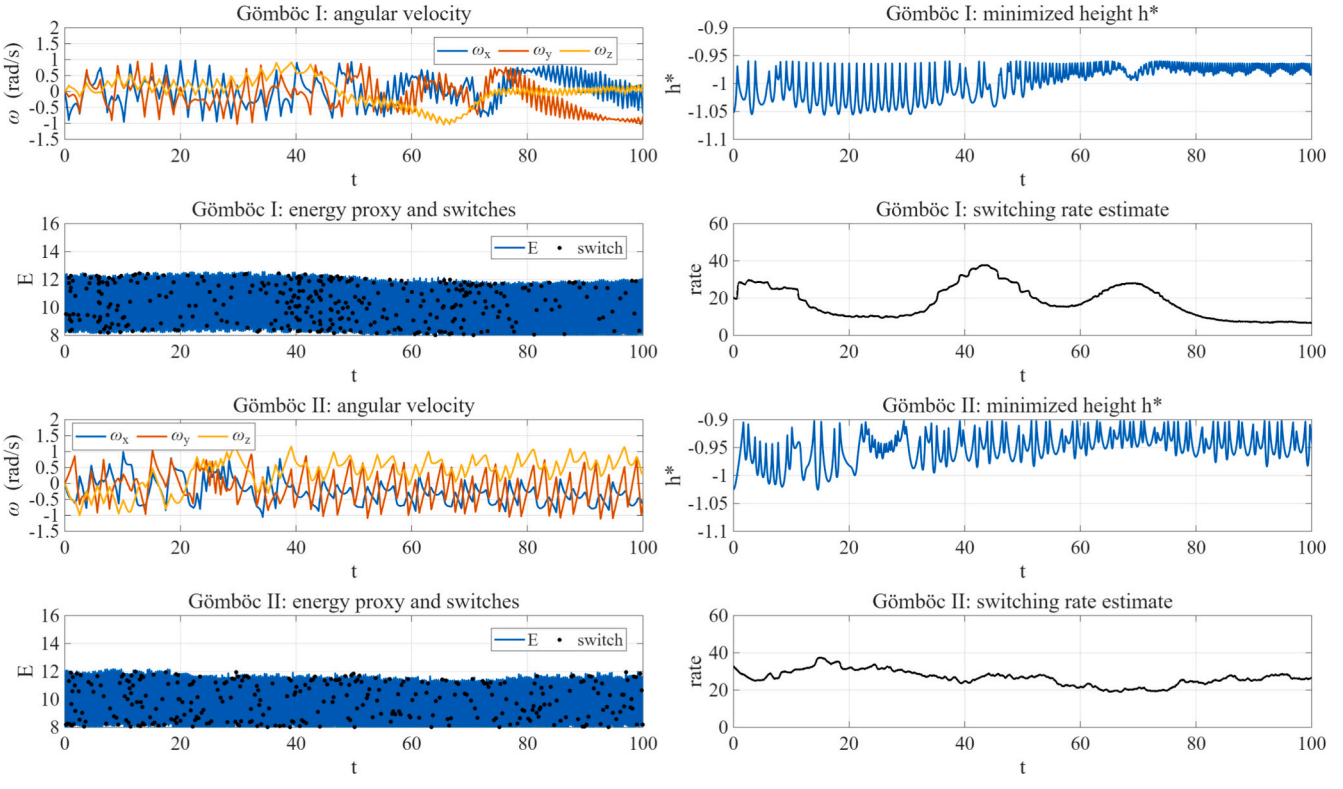

Fig. 5. Harmonic-excitation baseline time histories of angular velocity, minimized height, energy, and switching rate.

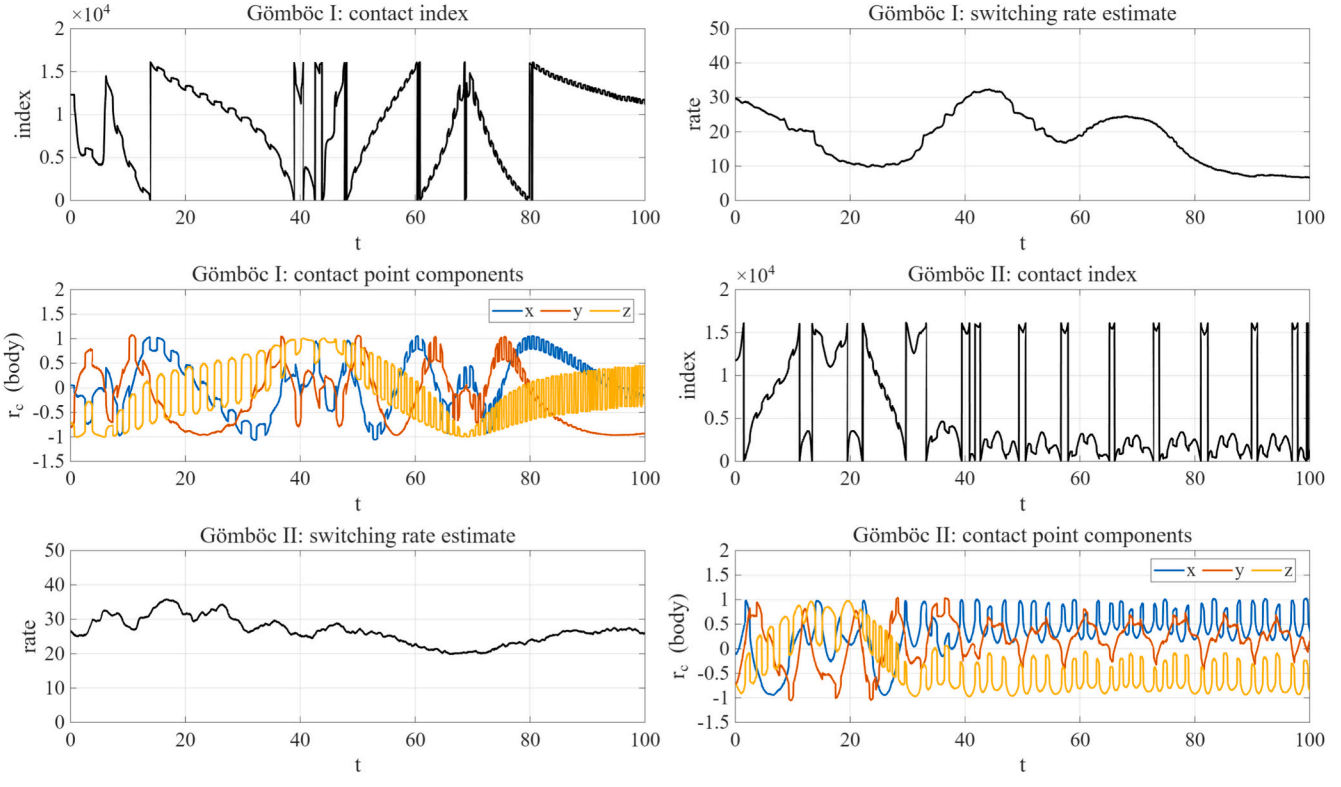

Fig. 6. Harmonic-excitation contact-point dynamics: index evolution, switching statistics, and contact coordinates.

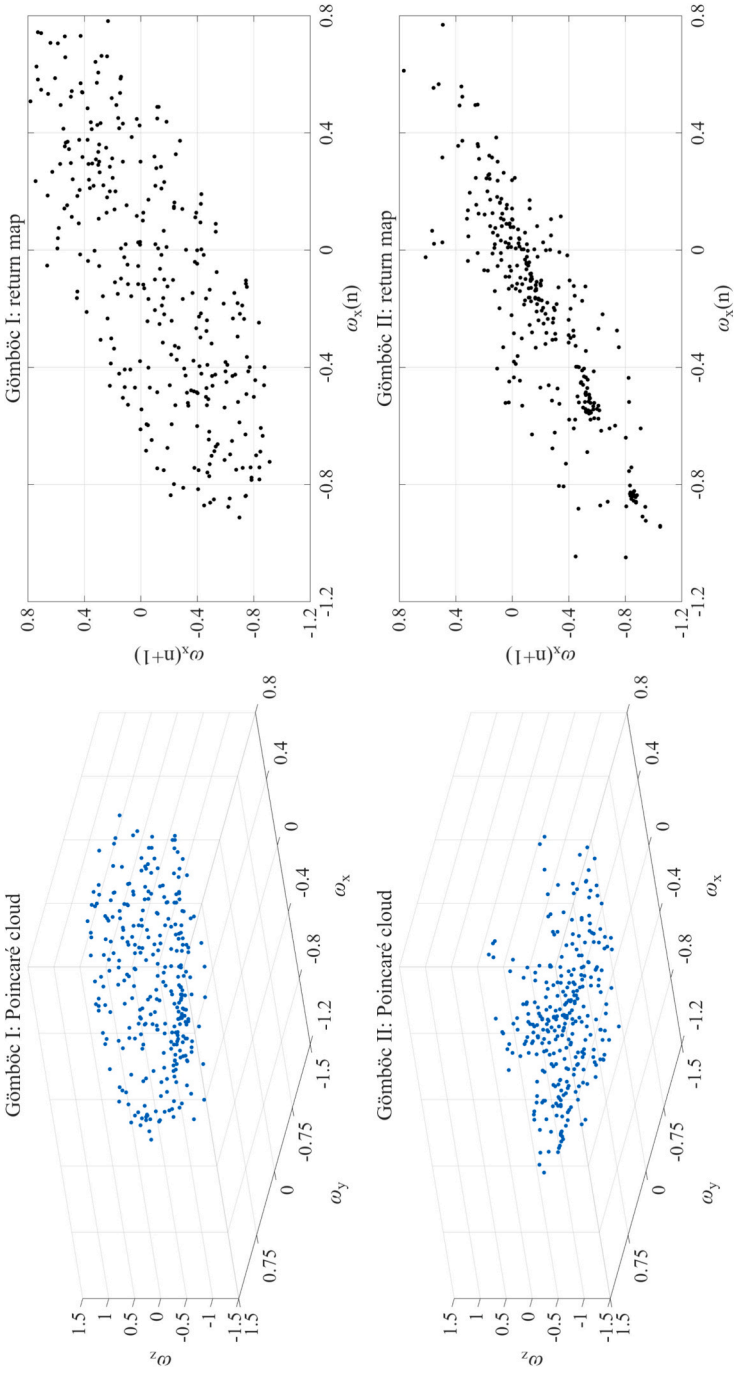

Fig. 7. Stroboscopic dynamics: Poincaré clouds and one-step return maps.

stronger inter-sample correlation in ω_x. At the same time, the map remains thick and multi-valued rather than collapsing to a single curve, which is incompatible with purely periodic motion and points to aperiodic dynamics on a complex invariant set. The clustering suggests that the system revisits preferred dynamical phases or contact selection regimes more regularly, consistent with the more persistent switching pattern observed in the time-domain contact diagnostics.

Overall, Fig. 7 shows that both morphologies generate stroboscopic responses that are not reducible to low-period motions at the baseline parameters. The differences in cloud geometry and return-map organization provide morphology-specific signatures of the underlying nonlinear mechanism. Gömböc I exhibits a more diffuse return-map structure, whereas Gömböc II exhibits a more organized but still multi-valued structure, supporting the conclusion that shape-dependent contact selection modulates the degree of coherence in the stroboscopic dynamics while maintaining an overall route toward chaotic behavior.

Fig. 8 presents complementary frequency-domain and state-space views of the baseline rocking dynamics for the two analytical Gömböcs. The left panels show the power spectrum of ω_x, computed from the time history of the body-frame angular-velocity component $\omega_x(t)$. The horizontal axis is frequency in hertz and the vertical axis is a power-like measure in arbitrary units. The right panels show phase portraits in the (ω_x, ω_z) plane, providing a compact projection of the trajectory in angular-velocity space that highlights geometric stretching, folding, and coherence properties that are not visible from single time traces.

For Gömböc I, the spectrum exhibits a broadband character with multiple peaks superimposed on a low-frequency background. The presence of several distinct peaks indicates that the response contains coherent oscillatory components, while the elevated spectral floor and the dense collection of smaller peaks indicate strong modulation and irregularity. This is consistent with a non-autonomous response in which periodic forcing interacts with morphology-induced contact selection to produce amplitude and phase variability. The corresponding phase portrait occupies an extended region and shows repeated sweeping motions with frequent direction changes, indicating that the dynamics explore a wide range of ω_x and ω_z values rather than remaining near a thin closed curve. Such a filled and folded structure is typical of aperiodic motion and suggests the coexistence of multiple dynamically active time scales.

For Gömböc II, the spectrum is more sharply organized, with several prominent narrow peaks concentrated at low frequencies and a comparatively weaker broadband background. This indicates a response with stronger quasi-periodic or multi-frequency content, where a small number of dominant components persist over time. At the same time, the spectrum is not purely discrete, since non-negligible power remains outside the main peaks, implying ongoing modulation rather than strict periodicity. The phase portrait for Gömböc II is more structured and anisotropic than for Gömböc I, showing clustered excursions along preferred directions in the (ω_x, ω_z) plane. This reflects a trajectory that repeatedly revisits similar angular-velocity configurations, which is consistent with the more regular contact-coordinate cycling and the more stationary switching activity observed in the contact diagnostics.

Taken together, Fig. 8 indicates that both morphologies exhibit complex rocking responses under the same forcing conditions, but with different spectral and geometric organization. Gömböc I displays stronger broadband features and a more space-filling phase portrait, suggesting more intense irregular modulation. Gömböc II displays more concentrated spectral peaks and a more organized phase portrait, indicating stronger residual coherence despite continued nonlinearity. These differences provide a frequency-domain and geometric complement to the stroboscopic evidence in the Poincaré and return-map diagnostics.

Fig. 9 quantifies sensitivity to initial conditions under baseline forcing by reporting both instantaneous per-period Lyapunov estimates and the cumulative maximal Lyapunov estimate for the two analytical Gömböcs. The instantaneous quantity λ_{inst} is computed once per forcing period from the growth of a small perturbation between two nearby trajectories, followed by renormalization to a fixed separation. The cumulative estimate $\lambda_{\max}$ is the running average of the same growth factors and provides a convergence diagnostic for the maximal Lyapunov exponent over increasing observation time. Positive values of $\lambda_{\max}$ indicate exponential separation of nearby trajectories and are widely used as evidence of chaotic dynamics in non-autonomous systems.

For Gömböc I, λ_{inst} rapidly rises from near zero and then fluctuates around a relatively stable level with moderate variability. The fluctuations reflect time-dependent stretching rates that change as the trajectory visits different regions of the contact selection landscape, while the absence of sustained negative excursions indicates persistent local divergence on average. The cumulative estimate $\lambda_{\max}$ converges quickly during the initial portion of the record and then stabilizes with only minor drift, indicating that the exponent is well resolved within the simulated time horizon. The converged value remains clearly above zero, supporting the interpretation that the baseline response corresponds to a chaotic attractor in the stroboscopic dynamics rather than to a long-period orbit with transient irregularity.

For Gömböc II, λ_{inst} exhibits stronger intermittency, with frequent downward spikes superimposed on a positive baseline level. These intermittent reductions correspond to intervals of reduced stretching, which are consistent with episodes of more coherent motion embedded within an overall irregular response. Despite this variability, the cumulative estimate $\lambda_{\max}$ again converges to a positive plateau after an initial transient and remains positive throughout the observation window. A small late-time adjustment is visible, which is consistent with the stronger intermittency of λ_{inst} and indicates that longer averaging windows can be beneficial for this morphology. Nevertheless, the persistence of a positive plateau supports robust sensitive dependence for Gömböc II under the same forcing conditions.

Overall, Fig. 9 provides a quantitative confirmation of chaos for both morphologies at baseline parameters. The comparison suggests that the two shapes have similar long-time average exponential divergence rates, while differing in short-time stretching variability. This difference aligns with the contact selection behavior observed in earlier figures, where Gömböc I exhibits more pronounced regime changes and Gömböc II exhibits more persistent switching activity, both of which can modulate finite-time Lyapunov fluctuations without eliminating the long-time positive exponent.

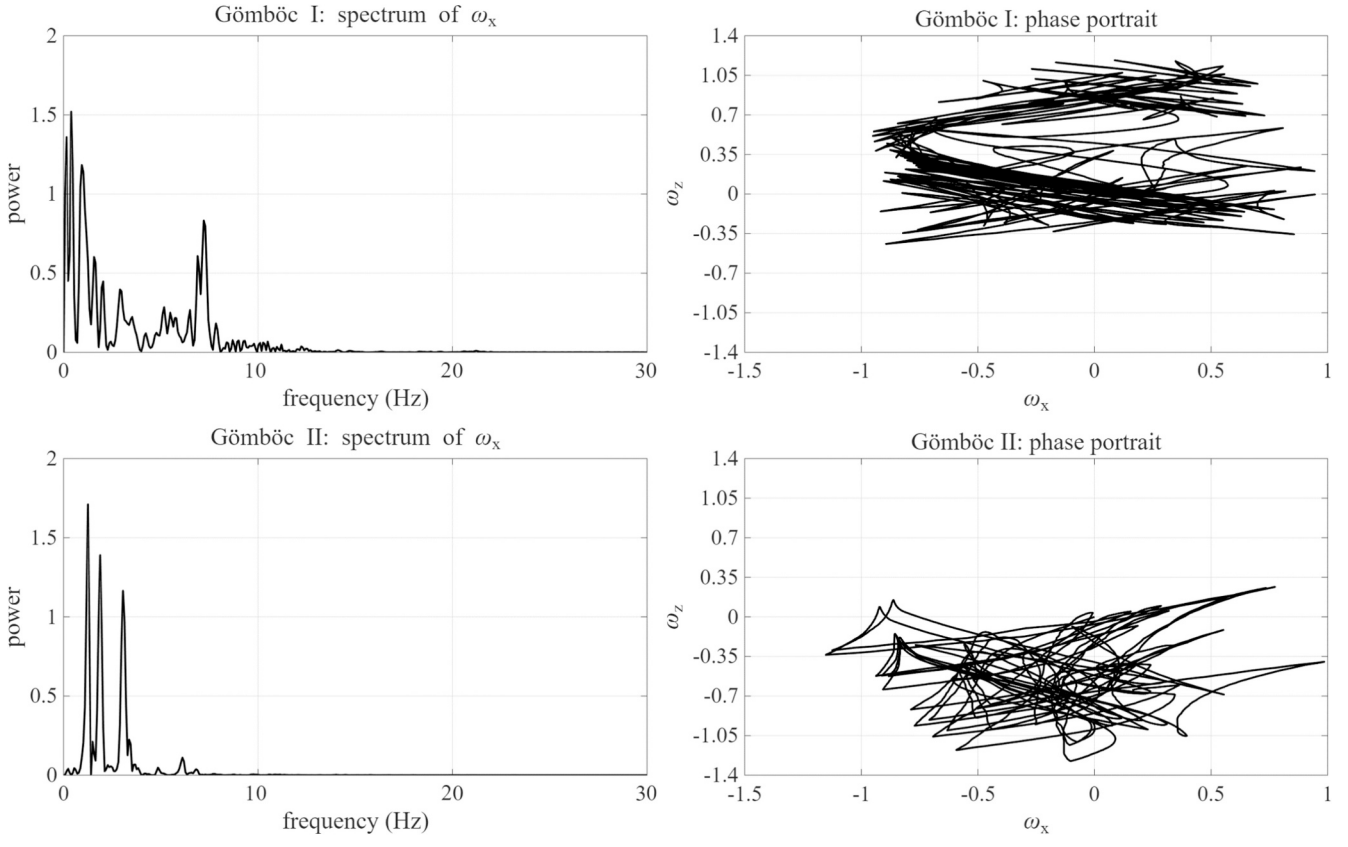

Fig. 8. Spectral signatures and phase portraits of the rocking motion.

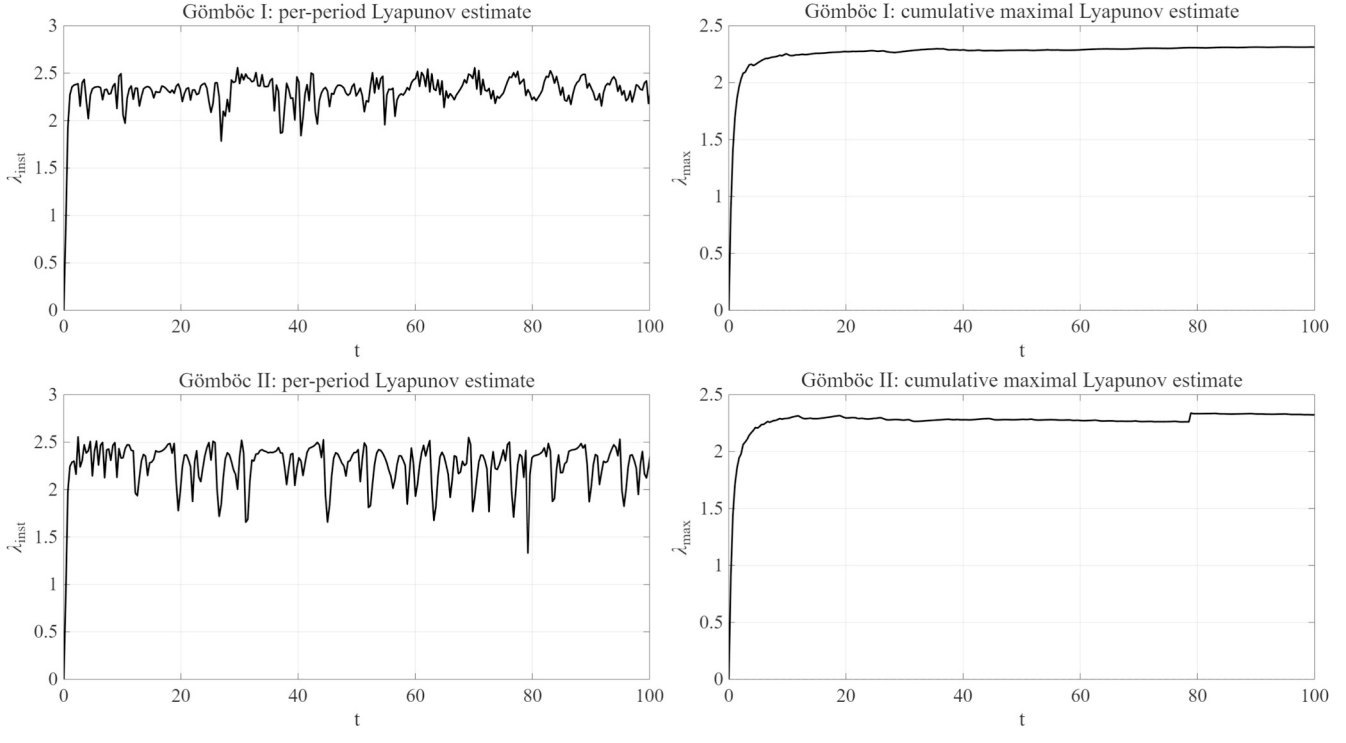

Fig. 9. Baseline maximal Lyapunov exponent: instantaneous and cumulative estimates.

8.3. Parameter-space organization and morphology comparison

Fig. 10 summarizes how the baseline response of Gömböc I reorganizes in the two-parameter plane spanned by the forcing angular frequency ω and the fundamental vertical-acceleration amplitude A_1, while holding the remaining excitation parameters fixed. Each panel reports a scalar metric computed from short integrations at each grid point, and the plotted surfaces are interpolated only for visualization. The upper-left panel shows the root-mean-square (RMS) angular speed, denoted here as ω_{RMS}, which measures the overall intensity of rotational motion. The upper-right panel shows the contact switching rate, defined as the number of changes in the active contact index per unit time. The lower-left panel shows the standard deviation of the stroboscopically sampled ω_x values, written as $\mathrm{std}(\omega_x)$, which provides a compact indicator of the spread of the stroboscopic response. The lower-right panel shows the mean minimized height, $\mathrm{mean}(h^*)$, which reflects how the active contact branches sample the height landscape on average.

Several robust trends are apparent. The ω_{RMS} surface exhibits pronounced ridges and valleys rather than monotone dependence on either parameter, indicating that response intensity is organized by resonance-like structures and nonlinear regime changes. Regions of increased ω_{RMS} tend to coincide with elevated switching rates, suggesting that more energetic rocking promotes more frequent contact-branch changes. At the same time, this correspondence is not one-to-one: there are parameter zones where switching remains relatively high while ω_{RMS} varies more mildly, implying that contact competition can remain active even without a large change in overall angular-speed level.

The Poincaré spread metric $\mathrm{std}(\omega_x)$ also displays a banded organization across the (ω, A_1) plane. Elevated stroboscopic variability aligns with regions where the switching rate surface is high, consistent with the interpretation that contact selection switching provides an effective stretching and folding mechanism in the stroboscopic map. Conversely, lower values of $\mathrm{std}(\omega_x)$ appear in patches where the switching rate is reduced, indicating parameter combinations that support more coherent, lower-variability dynamics.

The mean minimized height surface varies over a comparatively narrow range, reflecting that the body remains close to the plane and that the morphology is near spherical. Nevertheless, systematic variations are visible and correlate with the other metrics. Parameter regions with more negative $\mathrm{mean}(h^*)$ indicate that the active contact tends to occupy deeper minima of the height landscape, which can strengthen restoring torques and alter local stability. Where $\mathrm{mean}(h^*)$ shifts upward, the contact samples shallower parts of the landscape, which can facilitate switching between competing minima and amplify sensitivity.

Overall, Fig. 10 demonstrates that, for Gömböc I, the combination of forcing frequency and fundamental amplitude organizes a nontrivial response topology characterized by coupled variations in motion intensity, contact-switching activity, and stroboscopic dispersion. These surfaces provide a practical map for selecting parameter regions that are likely to exhibit strong irregular dynamics and for contrasting them with regions supporting more coherent rocking under the same morphology.

Fig. 11 investigates how the dynamics of Gömböc I depend on the second-harmonic component of the vertical excitation. The two control parameters are the second-harmonic acceleration amplitude A_2 and its phase shift ψ relative to the fundamental. The forcing frequency ω and the fundamental amplitude A_1 are held at their baseline values, so the observed variations are attributable to changes in the relative strength and timing of the second-harmonic contribution. The four panels report the same set of scalar metrics used previously: angular-speed intensity measured by ω_{RMS}, contact switching rate, the standard deviation of the stroboscopic ω_x sequence, and the mean minimized height $\mathrm{mean}(h^*)$.

The ω_{RMS} surface shows that adding a second harmonic modifies the response intensity in a strongly phase-dependent manner. Rather than increasing monotonically with A_2, the intensity surface exhibits ridges and localized maxima that shift with ψ, indicating constructive and destructive interference between the fundamental and second-harmonic contributions to the effective vertical acceleration. This behavior is expected in biharmonic excitation, where the timing of acceleration extrema relative to the body's rocking phase can either enhance or suppress the transfer of energy into rotational motion.

The switching-rate surface further indicates that the second harmonic can either promote or moderate contact selection activity depending on ψ. Regions of elevated switching form structured bands in the (A_2, ψ) plane, suggesting that contact-branch competition is not controlled solely by the magnitude of forcing but also by the phase alignment that determines when destabilizing intervals occur within each forcing cycle. The correspondence between increased switching rate and increased ω_{RMS} is present in several regions but is not universal, implying that the second harmonic can alter the contact selection landscape explored by the trajectory even when the global motion intensity changes only moderately.

The Poincaré spread metric $\mathrm{std}(\omega_x)$ exhibits comparatively smoother variation than in the (ω, A_1) scan, but still displays coherent phase-dependent modulation. Elevated values tend to align with parameter regions where the switching rate is high, consistent with the role of contact switching in broadening the stroboscopic distribution. Conversely, reduced stroboscopic spread occurs in patches where switching is weaker, indicating that a suitable choice of ψ can partially regularize the response despite the added harmonic component.

The mean minimized height surface varies over a narrow interval, reflecting the near-spherical geometry and the persistent single-contact constraint. Nonetheless, systematic changes across (A_2, ψ) are visible and track the regions where switching intensifies. Parameter regions where $\mathrm{mean}(h^*)$ shifts upward indicate that the active contact samples shallower portions of the height landscape more often, which is consistent with a greater likelihood of competition among nearby minima. Regions where $\mathrm{mean}(h^*)$ becomes more negative indicate more persistent occupation of deeper minima, which can stabilize contact selection and reduce switching.

Overall, Fig. 11 demonstrates that the second-harmonic forcing component acts as a sensitive control knob for Gömböc I, capable of reshaping both response intensity and contact selection activity through amplitude and phase. This phase dependence is particularly important for identifying parameter combinations that maximize irregular dynamics versus those that promote more coherent motion under biharmonic excitation.

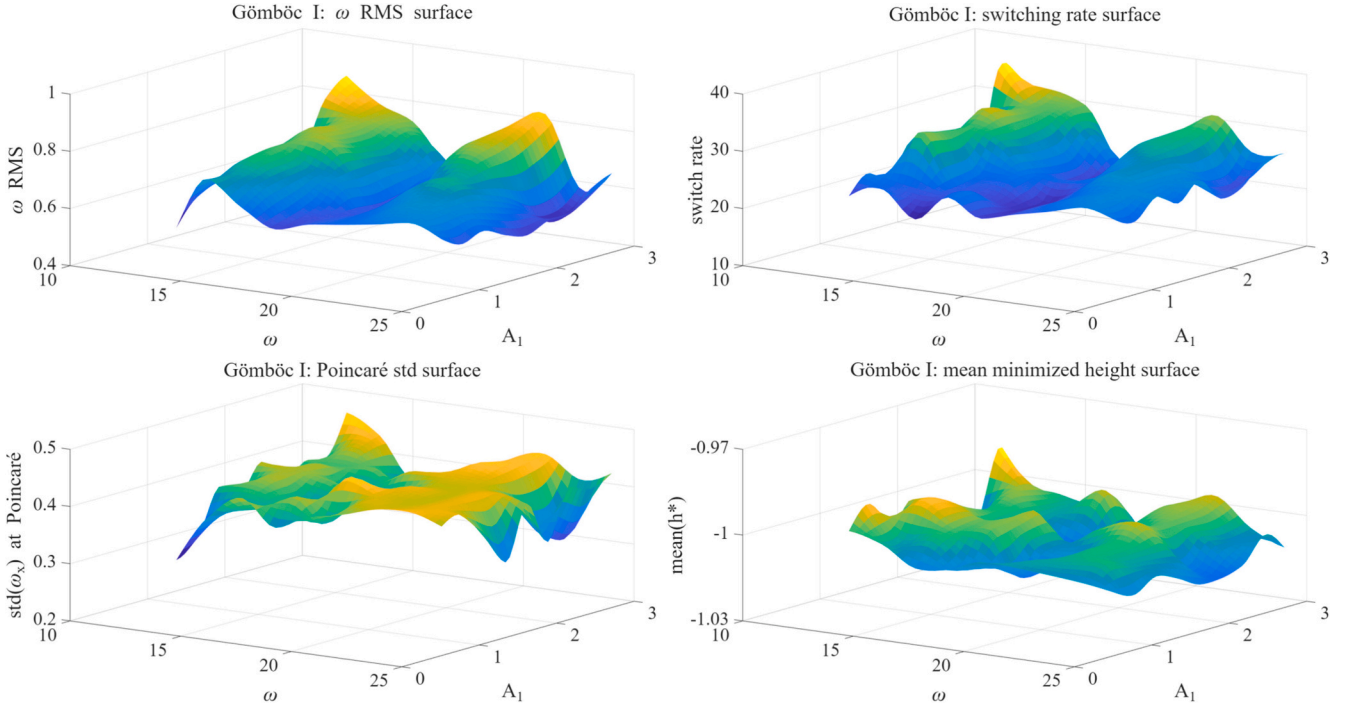

Fig. 10. Gömböc I response surfaces over forcing frequency and fundamental amplitude.

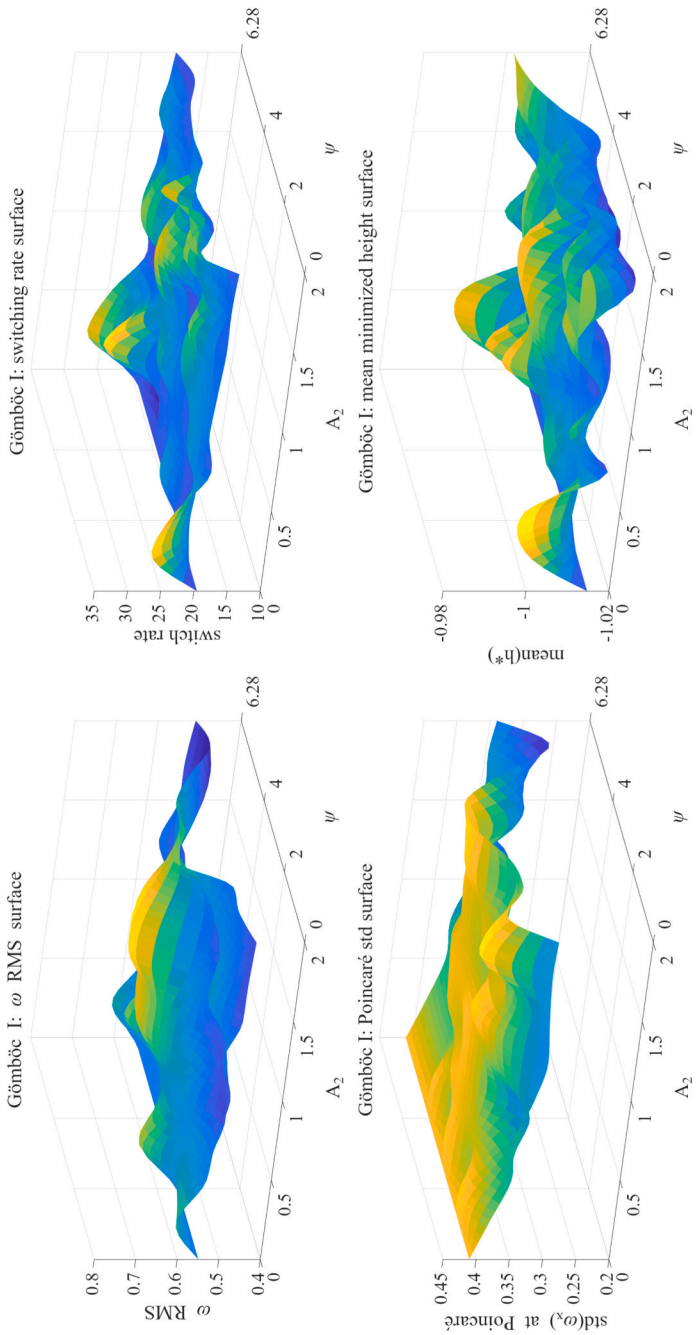

Fig. 11. Gömböc I response surfaces over second-harmonic amplitude and phase shift.

Fig. 12 maps the response of Gömböc II across the (ω, A_1) parameter plane, using the same four scalar metrics as in the corresponding Gömböc I scan. Compared with Gömböc I, Gömböc II exhibits a generally elevated baseline level of ω_{RMS} across the scanned region, with variations that are present but less ridge-dominated. This suggests that, for this morphology, the system sustains a relatively energetic rocking state over a wide range of ω and A_1, consistent with the more persistent contact switching seen in the baseline time histories. Local maxima and saddles remain visible, indicating that resonance-like tuning and nonlinear regime boundaries still organize the response, but the surface appears less fragmented into sharply separated high and low zones.

The switching-rate surface shows systematically higher levels than for Gömböc I, with broad regions where switching remains elevated rather than being confined to narrow ridges. This supports the interpretation that Gömböc II maintains stronger branch competition over much of the parameter plane, meaning that contact selection switching is less episodic and more robust to changes in forcing frequency and amplitude. The existence of extended plateaus also indicates that switching activity in this morphology is not simply a byproduct of increased ω_{RMS}, but reflects a geometry-driven propensity for multiple candidate minima to remain competitive across a broad range of attitudes.

The Poincaré dispersion metric $\mathrm{std}(\omega_x)$ displays a localized peak region embedded within a wider background of moderate values. This organization suggests that while the system often exhibits sustained irregularity, there exist parameter combinations where the stroboscopic variability becomes particularly large, consistent with transitions such as intermittency or crisis-like attractor expansions. In contrast to Gömböc I, where elevated dispersion is more broadly distributed, Gömböc II concentrates its strongest stroboscopic spreading into a smaller region, which aligns with the more structured return-map appearance and the more coherent spectral peaks observed at baseline.

The mean minimized height surface varies within a narrow band, but its undulations correlate with the other diagnostics. Parameter regions where $\mathrm{mean}(h^*)$ shifts upward are consistent with more frequent sampling of shallower competing minima, which can facilitate persistent switching. Regions where it shifts downward suggest more time spent near deeper minima, which can stabilize the contact selection locally even if overall rocking intensity remains high.

Overall, Fig. 12 shows that Gömböc II organizes the (ω, A_1) plane into broad domains of energetic motion and sustained contact switching, with localized zones of enhanced stroboscopic dispersion. This morphology-dependent topology contrasts with the more ridge-structured pattern of Gömböc I and reinforces the conclusion that the phase-function difference between the two analytical shapes influences how contact-branch competition persists under changes in forcing frequency and amplitude.

Fig. 13 characterizes how Gömböc II responds to variations in the second-harmonic excitation parameters, namely the amplitude A_2 and the phase shift ψ, while keeping the forcing frequency ω and the fundamental amplitude A_1 fixed at their baseline values. A primary observation is that ω_{RMS} varies only moderately across the (A_2, ψ) plane, forming a gently undulating surface with localized ridges. This indicates that, for Gömböc II, the second harmonic does not primarily act as a global intensity amplifier, but rather reshapes the response in a more selective manner. The most pronounced changes occur in restricted phase intervals, reflecting the importance of timing between the second-harmonic acceleration component and the internal rocking state. In this sense, ψ functions as an effective control parameter that can reorganize the response even when the overall angular-speed level remains within a narrow band.

The switching-rate surface remains elevated throughout the parameter plane, consistent with the morphology's tendency toward persistent contact-branch competition. Nevertheless, distinct bands and isolated crests are visible, showing that the second harmonic can further modulate switching activity beyond its baseline level. These phase-dependent features indicate that the second harmonic can either reinforce or partially suppress the conditions under which competing height minima exchange dominance. Importantly, the switching-rate variations are not strictly synchronized with the ω_{RMS} variations, supporting the conclusion that contact switching is governed not only by motion intensity but also by how the forcing waveform steers the system through regions of the contact selection landscape.

The Poincaré dispersion surface $\mathrm{std}(\omega_x)$ exhibits clearer phase sensitivity than the ω_{RMS} surface, with extended zones of increased dispersion separated by lower-variance regions. This behavior suggests that the second harmonic primarily influences the stroboscopic map through changes in variability and coherence rather than through large changes in average energy level. Regions of larger dispersion tend to coincide with elevated switching, which is consistent with the role of contact-branch changes in broadening the distribution of stroboscopic samples. Conversely, reduced dispersion patches indicate parameter combinations where the response is comparatively more coherent despite continued switching.

The mean minimized height surface varies over a very narrow range, but it remains informative as a geometric indicator. Subtle upward shifts in $\mathrm{mean}(h^*)$ align with regions where switching and dispersion are enhanced, consistent with more frequent occupation of shallower competing minima. Downward shifts correspond to parameter regions where the contact is biased toward deeper minima, which can locally stabilize the minimizer and reduce stroboscopic spread. Although the magnitude of these changes is small, their spatial organization across (A_2, ψ) provides a morphology-dependent signature of how the second harmonic biases the trajectory's sampling of the contact selection landscape.

Overall, Fig. 13 shows that for Gömböc II the second-harmonic amplitude and phase act primarily as modulators of contact selection activity and stroboscopic variability rather than as strong drivers of overall rotational intensity. This contrasts with the more ridge-dominated patterns observed for Gömböc I and reinforces the conclusion that morphology governs how biharmonic forcing organizes parameter-space regions associated with irregular dynamics.

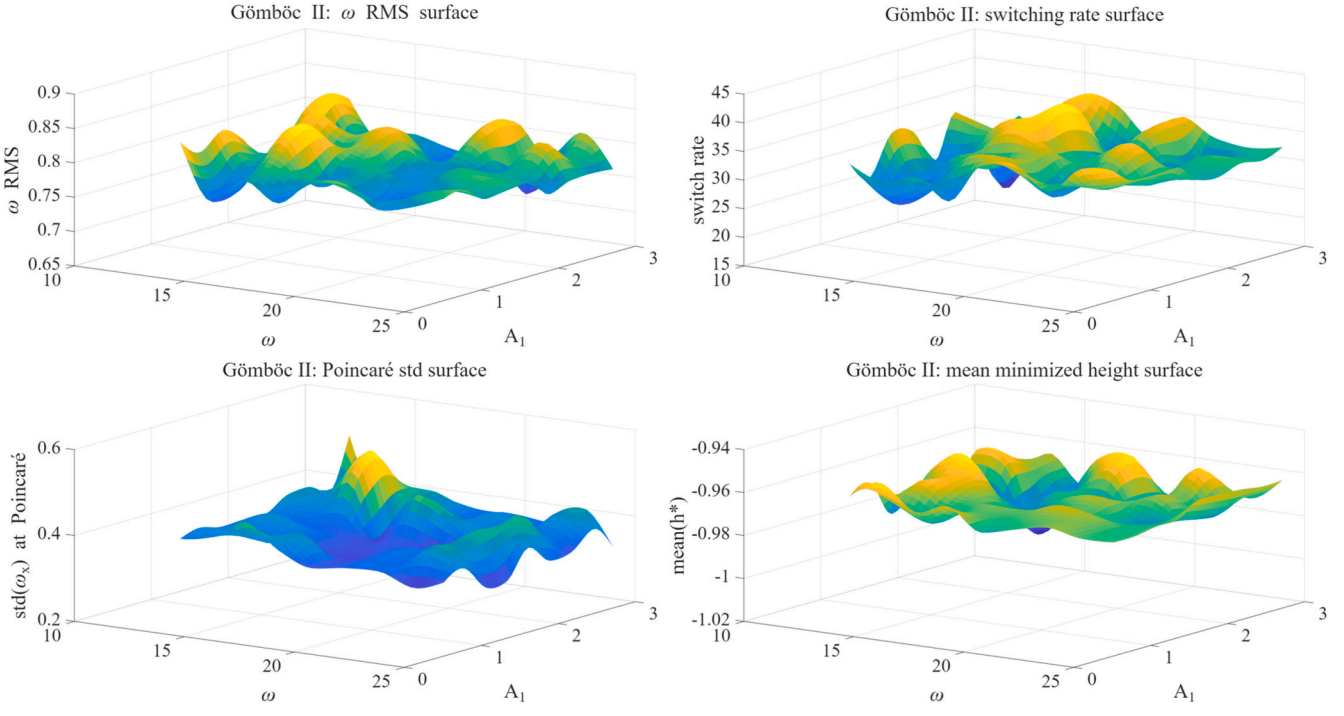

Fig. 12. Gömböc II response surfaces over forcing frequency and fundamental amplitude.

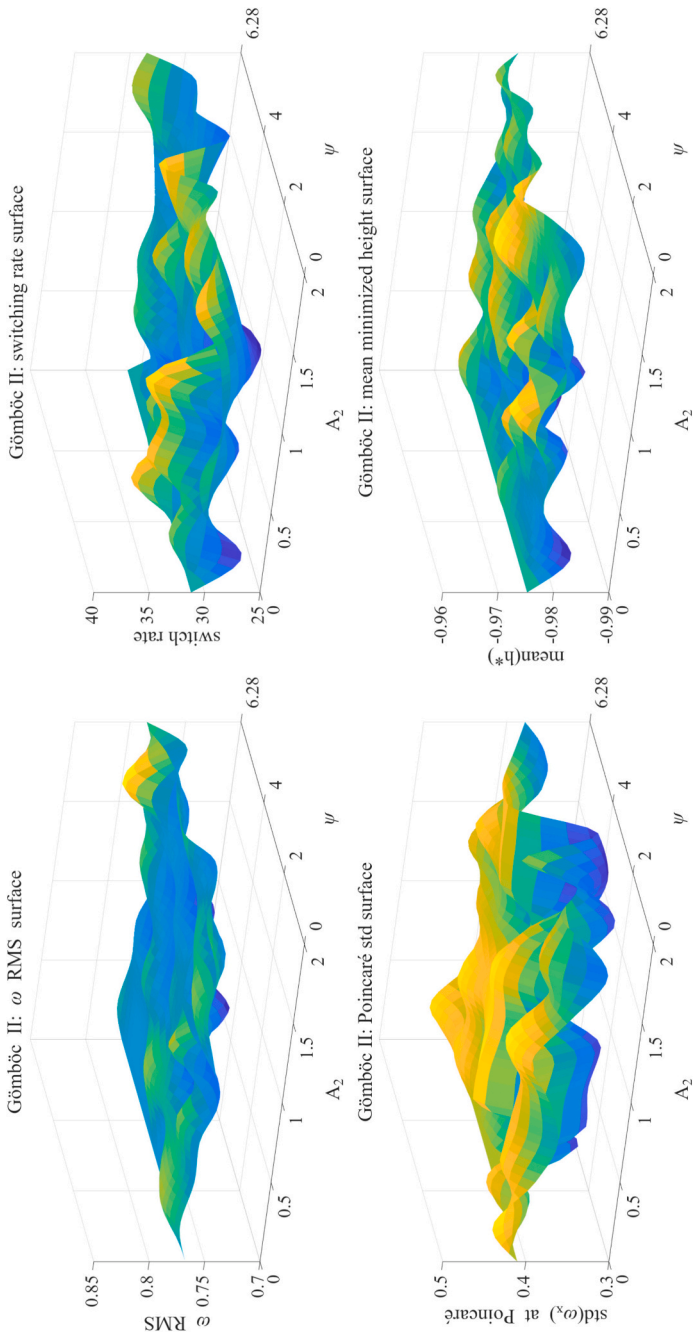

Fig. 13. Gömböc II response surfaces over second-harmonic amplitude and phase shift.

9. Conclusion

This study examined the forced rocking of two analytical Gömböc morphologies under biharmonic vertical excitation, with the instantaneous contact point determined by global height minimization on the rotated surface. The results show that even for smooth, strictly convex, near-spherical bodies, contact selection can induce deterministic switching between competing minimizing branches, providing a strong source of nonlinearity without relying on impacts or multi-contact constraints. Baseline simulations revealed bounded yet highly irregular responses in angular velocity, minimized height, and an energy proxy, with morphology-dependent differences in the temporal organization of switching activity and contact migration.

Across both morphologies, stroboscopic diagnostics and Lyapunov analyses consistently indicated chaotic dynamics at the baseline parameters. The Poincaré clouds and return maps exhibited extended, multi-valued structures incompatible with low-period responses, while the maximal Lyapunov exponent estimates remained positive after convergence, confirming sensitive dependence on initial conditions. Importantly, the two Gömböcs produced distinct short-time stretching patterns and different levels of coherence in spectral and phase-portrait signatures, linking the phase-function difference in the analytical morphologies to observable differences in attractor geometry and intermittency.

Finally, coarse parameter scans over forcing frequency and amplitudes, as well as over second-harmonic amplitude and phase shift, demonstrated that biharmonic excitation provides effective control over both response intensity and contact-switching statistics, but that the resulting organization in parameter space is strongly morphology-dependent. Gömböc I showed more ridge-structured and phase-sensitive response topology, whereas Gömböc II sustained broader domains of elevated switching with more selective amplification of stroboscopic dispersion. These findings support the conclusion that mono-monostatic morphology can act as an intrinsic chaos generator through contact selection, and that analytical shape design offers a systematic route to tune chaotic thresholds and response regimes in smooth convex-body rocking systems.

CRediT authorship contribution statement

Dong Feng: Writing – review & editing, Writing – original draft, Visualization, Validation, Software, Resources, Methodology, Investigation, Formal analysis, Data curation, Conceptualization, Funding acquisition, Project administration.

Declaration of competing interest

The author declares that he has no known competing financial interests or personal relationships that could have appeared to influence the work reported in this paper.

Acknowledgments

This research is supported by the China Scholarship Council (CSC., No. 202308080042). The author would like to thank two anonymous reviewers for their early comments, which significantly enhanced the quality of this paper.

Data availability

Data will be made available on request.

References

[1] Domokos G, Lángi Z, Várkonyi PL. A characterization of the symmetry groups of mono-monostatic convex bodies. Monatsh Math 2023;201(3):703–24. https://doi.org/10.1007/s00605-023-01847-w.
[2] Domokos G, Kovács F. Conway's Spiral and a Discrete Gömböc with 21 Point Masses. Am Math Mon 2023;130(9):795–807. https://doi.org/10.1080/00029890.2023.2241336.
[3] Arnol'd VI. Arnold's problems. 2nd ed. Berlin, New York, Moscow: Springer; PHASIS; 2005.
[4] Domokos G, Papadopulos J, Ruina A. Static equilibria of planar, rigid bodies: is there anything new? J Elast 1994;36(1):59–66. https://doi.org/10.1007/BF00042491.
[5] Shephard GC. Twenty Problems on Convex Polyhedra Part II. Math Gaz 1968;52(382):359–67. https://doi.org/10.2307/3611851.
[6] Varkonyi PL, Domokos G. Static Equilibria of Rigid Bodies: Dice, Pebbles, and the Poincare-Hopf Theorem. J Nonlinear Sci 2006;16(3):255–81. https://doi.org/10.1007/s00332-005-0691-8.
[7] Goldberg M, Guy RK. Stability oF polyhedra (J. H. Conway and R. K. Guy) SIAM Rev 1969;11(1):78–82. https://doi.org/10.1137/1011014.
[8] Várkonyi PL, Domokos G. Mono-monostatic bodies. Math Intell 2006;28(4):34–8. https://doi.org/10.1007/BF02984701.
[9] Domokos G, Várkonyi PL. Geometry and self-righting of turtles. Proc Biol Sci 2008;275(1630):11–7. https://doi.org/10.1098/rspb.2007.1188.
[10] Domokos G, Kovács F, Lángi Z, Regős K, Varga PT. Balancing polyhedra. Ars Math Contemp 2019;19(1):95–124. https://doi.org/10.26493/1855-3974.2120.085.
[11] Lángi Z. A solution to some problems of Conway and Guy on monostable polyhedra. Bull Lond Math Soc 2022;54(2):501–16. https://doi.org/10.1112/blms.12579.
[12] Zhang Y, Wang S, Fang H, Zhang Z, Yuan X. Investigation of the hysteresis behavior of a convex column brace based on buckling mode transition mechanism. Adv Mech Eng 2019;11(5). https://doi.org/10.1177/1687814019853690.
[13] Guan Y, Huang W, Wang H, Lu H, Yang H. Study on the stability of space sleeve stretching arm in the transition stage on non-continuous rigid surfaces based on scale optimization of elastic micro-convex bodies. Meccanica 2024;59(3):385–413. https://doi.org/10.1007/s11012-024-01757-7.
[14] Mathis L, Meroni C. Fiber Convex Bodies. Discrete Comput Geom 2023;70(4):1451–75. https://doi.org/10.1007/s00454-022-00451-3.

[15] Feng D. Multi-scale algorithm for controllable virtual aggregate generation in mesoscale modeling. Int J Mech Sci 2025;308:110978. https://doi.org/10.1016/j.ijmecsci.2025.110978.
[16] Feng D, Guan J, Fu C, Hu Y, Otto F, Hernandez AG, et al. Augmentation of 3D virtual aggregate database using deep convolutional Wasserstein generative adversarial networks. Adv Eng Inform 2026;69:103994. https://doi.org/10.1016/j.aei.2025.103994.
[17] Feng D. Parameter sensitivity in DEM of aggregates for road and construction materials. Adv Powder Technol 2025;36(12):105116. https://doi.org/10.1016/j.apt.2025.105116.
[18] Silva OM, Valentini F, Cardoso EL. Shape and position preserving design of vibrating structures by controlling local energies through topology optimization. J Sound Vib 2021;515:116478. https://doi.org/10.1016/j.jsv.2021.116478.
[19] Saviot L. Free Vibrations of Anisotropic Nano-Objects with Rounded or Sharp Corners. Nanomaterials 2021;11(7):1838. https://doi.org/10.3390/nano11071838.
[20] Feng D, Fu C, Zheng K, Wang T, Wang C. Numerical framework for asphalt pre-compaction optimization using a coarse-graining discrete element method (DEM). Powder Technol 2026;478:122486. https://doi.org/10.1016/j.powtec.2026.122486.
[21] Zhang Y, Needleman A. Characterization of plastically compressible solids via spherical indentation. J Mech Phys Solids 2021;148:104283. https://doi.org/10.1016/j.jmps.2020.104283.
[22] Feng D. A compactor-soil coupling model considering mechanical inertia and its delayed feedback active suspension control. International Journal of Non-Linear Mechanics 2025;179:105245. https://doi.org/10.1016/j.ijnonlinmec.2025.105245.
[23] Feng D. A DEM-based particle–force chain informatics framework for data-driven evaluation of pavement pre-compaction. Adv Eng Inform 2026;71:104402. https://doi.org/10.1016/j.aei.2026.104402.
[24] Pradhan C, Banerjee A, Roy R. Evolution of a 3D model for free-standing rigid blocks and its behavior under base excitations. International Journal of Non-Linear Mechanics 2022;142:103992. https://doi.org/10.1016/j.ijnonlinmec.2022.103992.
[25] Li Z, Wang T, Zhao C, Guo B, Ren Z, Jiang Z, et al. A coupled model of rolling process based on approximate rigid body model. Int J Mech Sci 2025;300:110433. https://doi.org/10.1016/j.ijmecsci.2025.110433.
[26] Burton MD, Chatzis MN. Modeling the Planar Rocking of a Rigid Body with Irregular Geometry. J Eng Mech 2023;149(9):4023054. https://doi.org/10.1061/JENMDT.EMENG-6956.
[27] Jiang L, Wang T, Huang Q-X. Resonance Analysis of Horizontal Nonlinear Vibrations of Roll Systems for Cold Rolling Mills under Double-Frequency Excitations. Mathematics 2023;11(7):1626. https://doi.org/10.3390/math11071626.
[28] Peng R, Zhang X, Shi P. Coupled Vibration Behavior of Hot Rolling Mill Rolls under Multinonlinear Effects. Shock Vib 2020;2020(1):1–14. https://doi.org/10.1155/2020/6104028.
[29] Feng D, Fu C, Liu P. A modified Johnson-Kendall-Roberts contact model for pavement engineering: Consideration of time-dependent surface energy. Powder Technol 2026;468:121701. https://doi.org/10.1016/j.powtec.2025.121701.
[30] Zhu Q, Ishitobi M. Chaotic vibration of a nonlinear full-vehicle model. Int J Solids Struct 2006;43(3–4):747–59. https://doi.org/10.1016/j.ijsolstr.2005.06.070.
[31] Feng D. A novel four-degree-of-freedom compactor–soil coupling model. Nonlinear Dyn 2026;114(8). https://doi.org/10.1007/s11071-026-12419-6.
[32] Zhao J, Zhao S, Luding S. The role of particle shape in computational modelling of granular matter. Nat Rev Phys 2023;5(9):505–25. https://doi.org/10.1038/s42254-023-00617-9.
[33] Jong PH de, Schwab AL, Mirzaali MJ, Zadpoor AA. A multibody kinematic system approach for the design of shape-morphing mechanism-based metamaterials. Commun Mater 2023;4(1):83. https://doi.org/10.1038/s43246-023-00410-2.
[34] Zhang Y, Needleman A. Influence of Assumed Strain Hardening Relation on Plastic Stress-Strain Response Identification From Conical Indentation. J Eng Mater Technol 2020;142(3). https://doi.org/10.1115/1.4045852.
[35] Legchenkova I, Frenkel M, Shvalb N, Shoval S, Gendelman OV, Bormashenko E. From Chaos to Ordering: New Studies in the Shannon Entropy of 2D Patterns. Entropy 2022;24(6):802. https://doi.org/10.3390/e24060802.
[36] Lu Y, Liu J, Zhang J, Wang J. Research on vibratory & oscillatory coexistence nonlinear dynamics based on drum-subgrade coupling model. International Journal of Non-Linear Mechanics 2023;157:104536. https://doi.org/10.1016/j.ijnonlinmec.2023.104536.
[37] Li R, Zhou X, Wu D, Wu S, Wang Y. Variable-Gain Subdivision Pressure Control Algorithm for Digital Valve Braking Systems via Partially Open Mode. IEEE Trans Ind Electron 2026:1–12. https://doi.org/10.1109/TIE.2026.3672823.
[38] Jia Y, Meng K, Jiang S, Kang J. Wear Prediction and Chaos Identification of Rigid Flexible Coupling Multi-Link Mechanisms with Clearance. Lubricants 2025;13(3):130. https://doi.org/10.3390/lubricants13030130.
[39] Ruan S, Chirikjian GS. Closed-form Minkowski sums of convex bodies with smooth positively curved boundaries. Comput Aided Des 2022;143:103133. https://doi.org/10.1016/j.cad.2021.103133.
[40] Zhang X, Li D, Grebogi C, Liu X. Dynamics of bouncing convex body. Chaos, Solitons Fractals 2024;183:114895. https://doi.org/10.1016/j.chaos.2024.114895.
[41] Regős K. Homogeneous, Monostatic Lattice Polyhedra, or the Magic Pyramid with 17 Sides. EpTud 2025;53(3–4):203–17. https://doi.org/10.1556/096.2025.00142.
[42] Almádi G, Mac G, Dawson RJ, Domokos G, Regős K. On equilibria of tetrahedra. Math Intell 2024;46(3):247–54. https://doi.org/10.1007/s00283-023-10294-2.
[43] Bryant J, Sangwin C. How Round Is Your Circle?: Where Engineering and Mathematics Meet. Princeton University Press; 2008.
[44] RESHETOV A. A unistable polyhedron with 14 faces. Int J Comput Geom Appl 2014;24(01):39–59. https://doi.org/10.1142/S0218195914500022.
[45] Sloan ML. Analytical Gomboc. ; preprint 2023. https://doi.org/14914.
[46] Kantz H. A robust method to estimate the maximal Lyapunov exponent of a time series. Phys Lett A 1994;185(1):77–87. https://doi.org/10.1016/0375-9601(94)90991-1.
[47] Li Y, Wei Z, Zhang W, Kapitaniak T. Melnikov-type method for chaos in a class of hybrid piecewise-smooth systems with impact and noise excitation under unilateral rigid constraint. Appl Math Model 2023;122:506–23. https://doi.org/10.1016/j.apm.2023.06.015.
[48] Awrejcewicz J, Holicke MM. Smooth and nonsmooth high dimensional chaos and the melnikov-type methods. New Jersey: WORLD SCIENTIFIC; 2007.